

---

# Demystifying Manifold Constraints in LLM Pre-training

---

Kang An<sup>1\*</sup>, Jiayang Li<sup>2\*</sup>, Donald Goldfarb<sup>3</sup>, Shiqian Ma<sup>1</sup>

<sup>1</sup>Rice University <sup>2</sup>Independent Researcher <sup>3</sup>Columbia University  
{kang.an, shiqian.ma}@rice.edu, jasonljx96@gmail.com, goldfarb@columbia.edu

## Abstract

The empirical success of large language model (LLM) pre-training relies heavily on heuristic stabilization techniques, such as explicit normalization layers and weight decay. While recent constrained optimization approaches that explicitly restrict weights may improve numerical stability and performance, the mechanism and motivation for adding constraints still remain elusive. This paper systematically demystifies the role of explicit manifold constraints in LLM pre-training. By introducing the Msign-Aligned Constrained Riemannian Optimizer (MACRO)—a provably convergent, single-loop optimization framework—our study disentangles weight regularization heuristics from interacting mechanisms like RMS normalization and decoupled weight decay. Theoretical analyses and comprehensive empirical evaluations reveal that manifold constraints independently bound forward activation scales and enforce stable rotational equilibrium, thereby subsuming the roles of these heuristic mechanisms. Evaluations on large-scale LLM architectures demonstrate that MACRO achieves highly competitive performance while rigorously preserving the theoretical guarantees of exact Riemannian optimization.

## 1 Introduction

Large language model (LLM) pre-training is increasingly shaped by mechanisms that control the scale and geometry of internal representations, including normalization layers, weight decay, and optimizer design. These mechanisms all implicitly regulate how activations and gradients propagate across depth, and they indeed achieve promising model performance. However, how much of training stability comes from the geometry effect of the weights, and how much is inherited from normalization layers and optimizer heuristics, is not fully understood. Recently, a line of work proposed optimization methods [1–10] that approximately constrain weights to structured sets, to control their scale. It is found that such constraints can empirically improve numerical stability and model performance. However, the reason behind this success remains poorly understood. While recent works have begun to explore manifold constraints, existing methods typically suffer from one of three critical limitations. First, some approaches rely on heuristic approximations [11] that lack rigorous geometric optimization guarantees. Second, some methods employ double-loop algorithms [6] that are computationally undesirable for large-scale pre-training. Finally, some methods based on Riemannian optimization techniques [7, 12] lack rigorous pre-training evaluations on modern LLM architectures and their practical scalability is thus not clear. More related works are in Appendix A.

The relation of explicit manifold constraints with other techniques for training stability (normalization layer, weight decay, etc.) is subtle in modern LLMs because weight constraints do not act in isolation. In architectures with RMS normalization, residual connections, and gated nonlinearities, the apparent effect of a geometric constraint may not be intuitive. A larger constraint radius may increase the

---

\*Equal Contribution.

raw scale of pre-normalized activations, but the normalization layer immediately rescales them away (see section 4.2). Moreover, while weight decay [13] was originally proposed to improve generalization, recent works [14–17] show that this technique also significantly shifts training dynamics. Because weight decay actively shrinks weights at each training step, applying an additional geometric constraint might appear redundant. Without disentangling these interacting mechanisms, it is hard to compare different constraints or to design principled constrained optimizers.

We aim to systematically study the effect of manifold constraints in LLM pre-training, and their interplay with normalization layers, weight decay, and algorithm heuristics. To this end, we consider explicitly constraining weight matrices to manifolds with prescribed geometry, such as spectral spheres, Frobenius spheres, and oblique manifolds. We explore the effect of applying these constraints from two perspectives: weight update dynamics and forward activation control. By explicitly tracking how these constraints govern both the amplification of layer outputs and the optimization trajectories, we isolate their intrinsic geometric control from the effects imposed by standard architectural heuristics. This comprehensive perspective directly addresses the fundamental question:

*Do the intrinsic geometric properties of manifold constraints subsume the heuristics widely used in modern LLM pre-training?*

Our contributions are summarized as follows:

1. **A Provable and Efficient Optimizer for Manifold Constrained LLM Pre-training (Section 3).** To systematically investigate the impact of manifold constraints in LLM pre-training, we propose a novel, single-loop optimizer: **M**sign-**A**ligned **C**onstrained **R**iemannian **O**ptimizer (**MACRO**). **MACRO** is essentially the Riemannian spectral SGD method with rigorous convergence guarantees and it bridges the gap between Riemannian optimization and practical large-scale deep learning.
2. **Differentiate the effects among different Manifold Constraints (Section 4.1).** We theoretically establish forward activation bounds for linear layers, demonstrating that the spectral sphere regulates worst-case activation scales, while the Frobenius sphere controls average-case behavior. Furthermore, our empirical comparison reveals that the Frobenius constraint consistently achieves lower validation loss than Oblique manifolds while maintaining similar internal training dynamics.
3. **Interplay with Normalization Layers (Section 4.2).** We empirically reveal a strong overlap between geometric constraints and explicit RMS normalization layer. By completely **removing the learnable normalization** from linear blocks, we demonstrate that **MACRO** maintains strict stability where standard optimizers may diverge, validating that manifold constraints naturally substitute the need for explicit normalization in the forward process.
4. **Interplay with Weight Decay (Section 4.3).** We theoretically and empirically reveal how manifold constraints fundamentally alter the training dynamics of LLMs. Specifically, we demonstrate that our geometric updates intrinsically lock the relative learning rate and govern the rotation angle between consecutive updates. This intrinsic geometric regulation formally fulfills the role of traditional weight decay, offering a principled alternative to heuristic penalty tuning.
5. **Empirical Justification (Section 5).** Comprehensive evaluations on standard LLM baselines (with standard architectures) show that **MACRO** achieves highly competitive, and often slightly superior, performance compared to strong methods such as MuonH [11], but with the added benefit of theoretical guarantees. Furthermore, compared to strict double-loop projection methods (e.g., SSO [6]), our single-loop approach offers a crucial efficiency-feasibility trade-off, achieving substantial computational savings with only a negligible relaxation in constraint exactness.

## 2 Notation and Preliminaries

**Notation.** Throughout this paper, we use capital bold letters such as  $\mathbf{W}$  to represent matrices and  $\mathbf{W}_{i,:}$ ,  $(\mathbf{W}_{:,j})$  to denote the  $i$ -th row ( $j$ -th column) of  $\mathbf{W}$ . Moreover,  $\|\mathbf{W}\|_F$  denotes the Frobenius norm of  $\mathbf{W}$ ;  $\|\mathbf{W}\|_2$  denotes the spectral norm of a matrix  $\mathbf{W}$ , and  $\|\mathbf{W}\|_*$  denotes the nuclear norm of  $\mathbf{W}$ , which is the dual norm of  $\|\mathbf{W}\|_2$ ;  $\|\mathbf{x}\|_2$  denotes the Euclidean norm of a vector  $\mathbf{x}$ ;  $\text{msign}(\mathbf{W})$  denotes the Matrix Sign Operator of matrix  $\mathbf{W}$ . That is,  $\text{msign}(\mathbf{W}) = \mathbf{U}\mathbf{V}^\top$ , where  $\mathbf{W} = \mathbf{U}\mathbf{\Sigma}\mathbf{V}^\top$  is the singular value decomposition of  $\mathbf{W}$ . For manifold  $\mathcal{M}$ , we use  $\mathbf{T}_{\mathcal{M}}\mathbf{W}$  to denote its tangent space at point  $\mathbf{W}$ . Further, we denote by  $\text{proj}_{\mathbf{T}_{\mathcal{M}}\mathbf{W}}(G)$  the projection of  $G$  onto the tangent space to the point  $\mathbf{W}$  on the manifold, and use  $\mathcal{P}_{\mathcal{M}}(X)$  to denote the projection (retraction) of  $X$  onto the manifold  $\mathcal{M}$ .

We use  $\nabla\mathcal{L}$  to denote the Euclidean gradient of  $\mathcal{L}$  and  $\nabla_{\mathcal{M}}\mathcal{L}(\mathbf{W})$  to denote the Riemannian gradient of  $\mathcal{L}$ . For embedded submanifolds considered in this paper, Riemannian gradient is the projection of the Euclidean gradient to the tangent space, i.e.,  $\nabla_{\mathcal{M}}\mathcal{L}(\mathbf{W}) = \text{proj}_{T_{\mathcal{M}}\mathbf{W}}(\nabla\mathcal{L}(\mathbf{W}))$ .

**Manifold Constraints.** We consider four constraint choices for the weight matrix  $\mathbf{W} \in \mathbb{R}^{D_{\text{out}} \times D_{\text{in}}}$ :

- **Frobenius Sphere [11]:** Bounds the total Frobenius norm via  $\mathcal{M}_F(R) = \{\mathbf{W} : \|\mathbf{W}\|_F = R\}$ .
- **Spectral Sphere [6]:** Constrains the maximum singular value via  $\mathcal{M}_S(R) = \{\mathbf{W} : \|\mathbf{W}\|_2 = R\}$ . Note that spectral sphere is actually **not a manifold**, however we could still compute the projections onto it and its tangent space. See the discussions in Appendix C.1 and Appendix B.1.
- **Input (resp. Output) Oblique Manifold [4]:** Restricts each input (resp. output) feature dimension to a fixed magnitude via  $\mathcal{M}_{O_{\text{in}}}(R_{\text{in}}) = \{\mathbf{W} : \|\mathbf{W}_{:,j}\|_2 = R_{\text{in}}, \forall j\}$  (resp.  $\mathcal{M}_{O_{\text{out}}}(R_{\text{out}}) = \{\mathbf{W} : \|\mathbf{W}_{i,:}\|_2 = R_{\text{out}}, \forall i\}$ ).

For each of these manifolds, we use  $\|\cdot\|_{\mathcal{M}}$  to denote the norm in their definition, i.e. for Frobenius sphere  $\|\cdot\|_{\mathcal{M}} = \|\cdot\|_F$ , for spectral sphere  $\|\cdot\|_{\mathcal{M}} = \|\cdot\|_2$ , for input oblique manifold,  $\|\cdot\|_{\mathcal{M}} = \max_j \|\cdot_{:,j}\| = \|\cdot\|_{1 \rightarrow 2}$  and for output oblique manifold  $\|\cdot\|_{\mathcal{M}} = \max_i \|\cdot_{i,:}\| = \|\cdot\|_{2 \rightarrow \infty}$ .

### 3 Our MACRO Algorithm

We consider the following manifold constrained LLM training problem:

$$\min_{\mathbf{W}} \mathcal{L}(\mathbf{W}) = \mathbb{E}_{\xi \sim \mathcal{D}} [\ell(\mathbf{W}, \xi)] \text{ s.t. } \mathbf{W} \in \mathcal{M}, \quad (1)$$

where  $\mathcal{M}$  is a manifold discussed in Sec 2. To solve (1), we propose a single-loop optimization framework, named **Msign-Aligned Constrained Riemannian Optimizer (MACRO)**. MACRO is a provably convergent Riemannian algorithm that maintains the spectral preconditioning benefits of the Muon [18] optimizer. The complete description of MACRO is given in Alg 1 and its main update is:

$$O_t = \text{msign}(\nabla_{\mathcal{M}}\mathcal{L}(\mathbf{W}_t)), \quad \mathbf{W}_{t+1} = \mathcal{P}_{\mathcal{M}}(\mathbf{W}_t - \eta_t c R \cdot O_t / (\|O_t\|_{\mathcal{M}} + \epsilon)), \quad (2)$$

where  $c > 0$  is a scaling hyperparameter, and  $\eta_t$  is the learning rate. This update scheme fundamentally differs from standard optimizers and the original Muon in the following key aspects:

- **Tangent Space Projection:** At each step, instead of using the raw moving average  $M_t$  as in standard Muon, we project it onto the tangent space of the constraint manifold at the current weight  $\mathbf{W}_t$  to obtain the valid Riemannian gradient  $\nabla_{\mathcal{M}}\mathcal{L}(\mathbf{W}_t)$ . For all manifold constraints mentioned in Section 2, such projection only requires standard matrix multiplications instead of computationally expensive sub-loops. The exact computations are detailed in Appendix B.1.
- **Riemannian Spectral Steepest Descent:** While Muon applies the matrix sign function to Euclidean gradients, MACRO evaluates the Linear Minimization Oracle (LMO) on the Riemannian gradient. This extracts the optimal steepest descent direction reflecting the local geometry of the manifold.
- **Update-Weight Ratio Alignment:** After obtaining the update direction  $O_t$ , we normalize and scale by projecting it back onto the manifold. This projection maintains the update-weight ratio strictly proportional to  $c \cdot \eta_t$ . Note that this double projection alters the magnitude of update direction and updated weight. Such projection operations also appear in SSO [6] and MuonH [11] algorithms. The strict ratio alignment explicitly provides an intrinsic regularization that formally subsumes traditional weight decay (theoretically analyzed in Section 4.3).
- **Manifold Projection/Retraction:** Following the parameter update, we apply a projection  $\mathcal{P}_{\mathcal{M}}$  (acting as a retraction) at every iteration to map the weights back onto the target constraint manifold  $\mathcal{M}$ , structurally preventing constraint drift. The exact computations are detailed in Appendix B.1.

**Convergence analysis.** Two assumptions are needed for the convergence analysis of MACRO.

**Assumption 1.** *We assume that  $\mathcal{M}$  is a compact  $C^3$  manifold.*

Note that this assumption does not hold for the spectral sphere  $\mathcal{M}_S(R)$ , which is not even a manifold, but it holds for the set  $\tilde{\mathcal{M}}_S(R) = \{\mathbf{W} : \|\mathbf{W}\|_2 = R, \sigma_1(\mathbf{W}) \geq \sigma_2(\mathbf{W}) + \epsilon\}$ , Frobenius sphere and the two oblique manifolds discussed in Section 2 (see Appendix C.1 and Yang and Lai [7] for a more detailed discussion). For the loss function  $\mathcal{L}$ , we also have the following assumption.

---

**Algorithm 1** Msign-Aligned Constrained Riemannian Optimizer (MACRO)

---

- 1: **Input:** Learning rate  $\eta_t$ , Manifold Constraint  $\mathcal{M}$ , Hyperparameters  $\beta, R, c, T$
  - 2: **for**  $t = 0, 1, \dots, T$  **do**
  - 3:    $G_t = \nabla \ell(\mathbf{W}_t, \xi_t)$
  - 4:    $M_t = \beta M_{t-1} + (1 - \beta)G_t$
  - 5:    $\Phi_t = \text{proj}_{\mathcal{T}_{\mathcal{M}}}\mathbf{W}_t(M_t)$  ▷ Projection to the Tangent Space
  - 6:    $O_t = \text{msign}(\Phi_t)$  ▷ Compute the steepest descent direction via LMO
  - 7:    $\tilde{\nabla}_t = cR \cdot O_t / (\|O_t\|_{\mathcal{M}} + \epsilon)$  ▷ Normalization and Scaling
  - 8:    $\mathbf{W}_{t+1} = \mathcal{P}_{\mathcal{M}}(\mathbf{W}_t - \eta_t \cdot \tilde{\nabla}_t)$  ▷ Descent Step and Manifold Projection
  - 9: **end for**
- 

**Assumption 2.** We assume the loss function  $\mathcal{L}$  is lower bounded by  $\mathcal{L}^*$ , and has  $L$ -Lipschitz continuous gradient, and the stochastic loss  $\ell(W, \xi)$  satisfies: (i) the stochastic gradient is unbiased, i.e.  $\mathbb{E}_{\xi} \nabla \ell(W, \xi) = \nabla \mathcal{L}(W)$ ; (ii) the variance is bounded, i.e.,  $\mathbb{E}_{\xi} \|\nabla \ell(W, \xi) - \nabla \mathcal{L}(W)\|_F^2 \leq \sigma^2$ .

Under these two assumptions, we have the following theorem.

**Theorem 1.** Suppose the manifold  $\mathcal{M}$  and the loss function  $\mathcal{L}$  satisfy Assumptions 1 and 2. Denote  $\Delta = \mathcal{L}(\mathbf{W}_0) - \mathcal{L}^*$ . By setting  $\beta = 1 - 1/\sqrt{T}$ ,  $\eta_t = \eta = \Omega(\sqrt{\Delta}/(LT^{3/2}))$ , the sequence  $\{\mathbf{W}_t\}$  generated by Algorithm 1 satisfies (constants related to dimension are omitted in  $\mathcal{O}$ ):

$$\min_{t=0, \dots, T-1} \mathbb{E} \|\nabla_{\mathcal{M}} \mathcal{L}(\mathbf{W}_t)\|_* \leq \mathcal{O}\left(\sqrt{L\Delta}\sigma T^{-1/4}\right).$$

This matches the  $\mathcal{O}(T^{-1/4})$  rate for general nonconvex smooth stochastic optimization [19].

## 4 Effects of Manifold Constraints on Training Dynamics

In this section, we discuss the relation of the explicit manifold constraint with two normalization mechanisms – weight decay and normalization layers – and show that manifold constraint is a competitive alternative that substitutes these two mechanisms.

### 4.1 Activation Scale Control via Spectral Sphere or Frobenius Sphere Constraints

In this subsection, we analyze and compare Frobenius and spectral spheres, and output/input Oblique manifolds. The major benefit of weight constraints is controlling the scale of activations. Consider a single linear layer  $\mathbf{Y} = \mathbf{X}\mathbf{W}^T$ , where  $\mathbf{X} \in \mathcal{R}^{T \times D_{\text{in}}}$ ,  $\mathbf{Y} \in \mathcal{R}^{T \times D_{\text{out}}}$  and  $\mathbf{W} \in \mathcal{R}^{D_{\text{out}} \times D_{\text{in}}}$  for a sequence of length  $T$ . Following Yang et al. [20] and Su [21], our goal is for the forward pass to maintain a constant root-mean-square (RMS) norm:  $\|\text{vec}(\mathbf{Y})\|_{\text{RMS}} = \Theta(1)$ . We can express this sequence-level operation using the Kronecker product:  $\text{vec}(\mathbf{Y}) = (\mathbf{W} \otimes I_T) \text{vec}(\mathbf{X})$ . Importantly, the spectral norm remains invariant under this expansion ( $\|\mathbf{W} \otimes I_T\|_2 = \|\mathbf{W}\|_2$ ), thus explicitly constraining  $\|\mathbf{W}\|_2$  directly bounds the activation amplification.

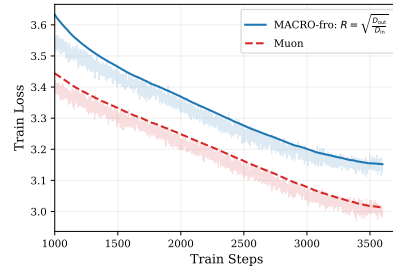


Figure 1: Train loss for 120M QWEN3-like model.

**Why the Worst-Case Bound Fails for Frobenius Constraints.** For Frobenius sphere, one way to bound the output scale is the sub-multiplicative property of the Frobenius norm:  $\|\mathbf{Y}\|_F \leq \|\mathbf{X}\|_F \|\mathbf{W}\|_F$ . Assuming  $\|\text{vec}(\mathbf{X})\|_{\text{RMS}} = \Theta(1)$ , we obtain the following worst-case output bound:

$$\|\text{vec}(\mathbf{Y})\|_{\text{RMS}} \leq \sqrt{D_{\text{in}}/D_{\text{out}}} \|\mathbf{W}\|_F \|\text{vec}(\mathbf{X})\|_{\text{RMS}}.$$

To ensure  $\|\text{vec}(\mathbf{Y})\|_{\text{RMS}} = \Theta(1)$ , we must set the constraint radius to  $\|\mathbf{W}\|_F = \Theta(\sqrt{D_{\text{out}}/D_{\text{in}}})$ . But, this worst-case radius may hurt pre-training (see Fig 1) due to the following reasons.

- **Rank and Context Collapse:** The equality in our bound relies on the Cauchy-Schwarz inequality:  $\langle x_i, w_j \rangle^2 \leq \|x_i\|_2^2 \|w_j\|_2^2$ . This equality only holds if all token representations  $x_i$  share the exact same direction and  $\mathbf{W}$  collapses to a rank-1 matrix. Therefore, designing a constraint around this worst-case bound assumes that the LLM completely lost its representational capacity.
- **Severe Capacity Attenuation:** Consider an initialization where  $\mathbf{W} \sim \mathcal{N}(0, \sigma^2)$ . Random matrix theory [22] suggests that as  $D_{\text{in}}, D_{\text{out}} \rightarrow \infty$ , the ratio of the Frobenius norm to the spectral norm converges:  $\frac{\|\mathbf{W}\|_F}{\|\mathbf{W}\|_2} \rightarrow \frac{\sqrt{D_{\text{out}}}}{1 + \sqrt{D_{\text{out}}/D_{\text{in}}}}$ . Therefore, artificially restricting  $\|\mathbf{W}\|_F = \Theta(\sqrt{\frac{D_{\text{out}}}{D_{\text{in}}}})$  forces the spectral norm to shrink to  $\|\mathbf{W}\|_2 = \Theta(\frac{1}{\sqrt{D_{\text{in}}}})$ . This reduces the effective capacity of the linear layer by a factor of  $\frac{1}{\sqrt{D_{\text{out}}}}$ , causing severe forward-pass attenuation and training instability.

The true mechanism of the Frobenius constraint becomes clear when we analyze **average-case behavior** governed by the empirical input covariance,  $\Sigma_{\mathbf{X}} = \frac{1}{T} \mathbf{X}^\top \mathbf{X}$ . During training, optimization dynamics continuously change this covariance. Therefore, we evaluate the average output RMS norm using the trace formulation:  $\mathbb{E}_{\mathbf{X}}[\|\text{vec}(\mathbf{Y})\|_{\text{RMS}}^2] = \frac{1}{D_{\text{out}}} \text{tr}(\Sigma_{\mathbf{X}} \mathbf{W}^\top \mathbf{W})$ . We tightly bound this trace in Proposition 1, which summarizes how these two constraints control activation scales differently (see Appendix C.2 for proof).

**Proposition 1** (Radius Selection for Activation Control). *Assume the input activations satisfy  $\|\text{vec}(\mathbf{X})\|_{\text{RMS}} = \Theta(1)$ . To maintain stable output scales, the constraint radii are determined by two different mechanisms:*

- **Spectral Sphere:** The spectral constraint controls the worst-case weight scale. To guarantee the strict upper bound  $\|\text{vec}(\mathbf{Y})\|_{\text{RMS}} = \mathcal{O}(1)$ , we set the spectral radius to  $R_{\text{spec}} = \Theta(\sqrt{D_{\text{out}}/D_{\text{in}}})$ .
- **Frobenius Sphere:** The Frobenius constraint controls the expected output scale. Assume
  1. The weight matrix maintains a high stable rank, i.e.  $\|\mathbf{W}\|_2^2 \leq \frac{\kappa}{\min\{D_{\text{in}}, D_{\text{out}}\}} \|\mathbf{W}\|_F^2$  for a structural constant  $\kappa = \Theta(1)$  (see Figure 2, this is commonly observed in the experiments).
  2. The context length typically exceeds the hidden dimension (which ensures the empirical input covariance remains strictly positive definite), and  $\lambda_{\min}(\Sigma_{\mathbf{X}}) = \Omega(1)$  almost surely.

To ensure  $\mathbb{E}_{\mathbf{X}}[\|\text{vec}(\mathbf{Y})\|_{\text{RMS}}] = \Theta(1)$ , we set a larger Frobenius radius:  $R_{\text{fro}} = \Theta(\sqrt{D_{\text{out}}})$ .

Additionally, we introduce a tunable hyperparameter  $r = \Theta(1)$  to establish the practical constraint radii. For the Frobenius and spectral constraints, we directly adopt  $R_{\text{spec}} = r\sqrt{D_{\text{out}}/D_{\text{in}}}$  and  $R_{\text{fro}} = r\sqrt{D_{\text{out}}}$ . For the oblique manifold constraints, we derive their radii by matching their overall Frobenius norm to the radius of the Frobenius sphere. Table 1 summarizes the practical radii for all manifolds. In Appendix C.2, we show that these radius choices align with existing literature.

**Oblique vs. Frobenius Constraints** Based on the aforementioned radii, a preliminary comparison reveals that the Frobenius constraint consistently achieves lower validation loss than Oblique constraints across various learning rates (Figure 11 (a)). Furthermore, their internal training dynamics—including spectral and maximum row/column norms—closely match (Figure 11 (b)-(d)). Since Oblique constraints offer no performance advantage comparing to Frobenius, we omit them in the remainder of the paper and only focus on the spectral and Frobenius sphere constraints. Detailed discussions are deferred to Appendix D.4.

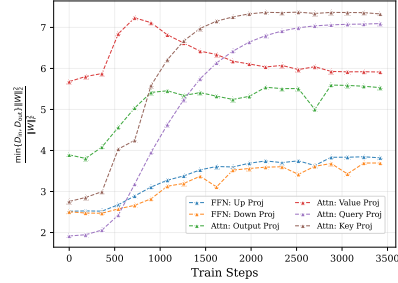


Figure 2: Empirical validation of  $\kappa$ .

Table 1: Practical constraint radii.

Manifold	Radius Setting
Spectral Sphere	$r\sqrt{D_{\text{out}}/D_{\text{in}}}$
Frobenius Sphere	$r\sqrt{D_{\text{out}}}$
Output Oblique	$r$
Input Oblique	$r\sqrt{D_{\text{out}}/D_{\text{in}}}$

🔑 **Key Takeaway:** *The functions of the spectral and Frobenius spheres differ: the former bounds the worst-case, while the latter bounds the average-case, activation. Both regulate the output scale to  $\Theta(1)$ .*

## 4.2 Interplay between Manifold Constraints and Normalization Layers

In standard LLM architectures, normalization layers [23–27] explicitly control the forward activation scale. For example, the RMSNorm layer [28] uses a learnable affine parameter,  $\gamma$ , to scale activations. However, as Proposition 1 establishes, manifold constraints govern exactly the same scale. Because both mechanisms control the activation scale, they interact during training. Figure 3 illustrates this interaction. When we increase the manifold constraint radius  $R$  (which presumably allows for larger pre-norm activations), the optimizer automatically shrinks the affine parameter  $\gamma$ . This keeps the final activation scale constant for subsequent layers, which suggests that standard RMSNorm layers are redundant when manifold constraint is present. To verify this, we **completely remove the learnable RMS normalization** layers from the model structure and test the algorithm performances. This allows us to evaluate the standalone stabilizing capability of explicit manifold constraints during LLM pre-training. Manifold constraints on weights explicitly bound the output scale of linear layers to  $\Theta(1)$ . To maintain an input scale of  $\|\text{vec}(\mathbf{X})\|_{\text{RMS}} = \Theta(1)$  for each layers, we still insert a parameter-free RMSNorm immediately after the attention block, alongside QK-norm to stabilize the pre-softmax logits. In addition, for the SwiGLU activation, the Hadamard product fundamentally disrupts linear stability (Multiplying two matrices of scale  $c$  element-wise yields a  $c^2$  scale, which cascades exponentially across  $L$  layers to cause INF values). To prevent this without learnable norms, we introduce Norm-Gated SwiGLU. This modification normalizes the Swish branch before the multiplication:

$$\mathbf{Y} = (\text{Swish}(\mathbf{X}\mathbf{W}_1^\top) / \|\text{Swish}(\mathbf{X}\mathbf{W}_1^\top)\|_{\text{RMS}}) \odot (\mathbf{X}\mathbf{W}_2^\top). \quad (3)$$

Finally, we apply a parameter-free normalization after the initial embedding layer. This step guarantees the  $\Theta(1)$  input scale for the first transformer block.

By using only **parameter-free normalizations** described above, we force the optimizer to control all activation magnitudes alone. We test this setup by training a 330M QWEN3-like model (with RoPE, GQA, and SwiGLU) across various learning rates (see Appendix D.1 for the detailed experimental settings). Table 3 shows that, without learnable normalization layers, standard Muon diverges (NaN) at the standard learning rates used by the RMSNorm baseline. In contrast, MACRO prevents this failure. It successfully scales to these standard learning rates, maintaining stability and achieving validation loss comparable to the fully normalized baseline. Furthermore, Table 3 shows that the Spectral constraint outperforms the Frobenius constraint. This result supports our analysis in Proposition 1 that, without the safety component of explicit normalization layers, the strict worst-case activation bound of the Spectral sphere provides better stability than the Frobenius sphere.

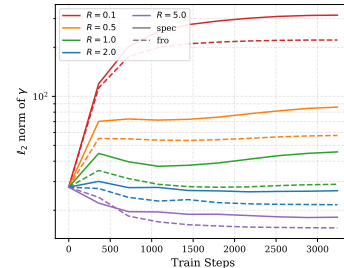


Figure 3: Evolution of  $\ell_2$  norm of  $\gamma$  during training.

Table 2: Architecture Comparison

	Standard Baseline	RMSNorm-Free
Activation	SwiGLU	Eq (3)
Attn:Norm	False	True
RMSNorm Layer	True	False

Table 3: Validation loss for QWEN3-like 330M pre-training without learnable normalization layers.

Optimizer	Learning Rate				
	$3 \times 10^{-3}$	$5 \times 10^{-3}$	$7 \times 10^{-3}$	$1 \times 10^{-2}$	$3 \times 10^{-2}$
Muon (baseline)	2.912	2.849	2.823	2.813	NaN
MACRO-fro (Ours)	2.901	2.825	2.787	<b>2.758</b>	2.781
MACRO-spec (Ours)	2.820	2.768	2.747	<b>2.739</b>	2.819

While our MACRO-spec remains strictly stable on parameter-free architecture, its validation loss is roughly  $0.02^\dagger$  higher than MACRO-spec on standard baseline (Table 2). This marginal gap is expected: learnable normalizations use layer-specific parameters ( $\gamma$ ) that adapt during training. Our current MACRO implementation, however, uses a single global constraint radius  $r$  for all layers. To close this performance gap, future work should co-design layer-specific geometric constraints based on the dynamics of different transformer modules.

🔑 **Key Takeaway:** Without learnable normalization layers, Muon may diverge. In contrast, our constrained optimizer MACRO shows better numerical stability and performance even when all learnable normalization layers are removed.

### 4.3 Interplay between Manifold Constraints and Weight Decay

Decoupled weight decay [13] is standard practice in model training. Recent works [14, 15, 17, 29, 30] show that the implicit regularization of weight decay relies on two geometric mechanisms: First, with weight decay, the *relative learning rate*, defined as the magnitude ratio  $\eta_{\text{rel},t} = \|\Delta \mathbf{W}_t\|/\|\mathbf{W}_t\|$  is bounded. This ratio is a crucial metric for optimization stability [6, 11]; Second, with weight decay, the late stage training only changes the *rotational angle* of consecutive updates, defined as  $\theta_t = \angle(\mathbf{W}_{t+1}, \mathbf{W}_t)$  [15].

However, standard weight decay achieves these geometric properties heuristically. For example, Defazio [14] shows that applying weight decay with a coefficient  $\lambda$  in SGD results in  $\eta_{\text{rel},t} \approx \sqrt{2\lambda}/\eta_t$ . In addition, the learning rate  $\eta_t$  typically decays during training. Consequently this relative learning rate constantly changes, causing the gradient norm to amplify near the end of training for optimizers like AdamW and SGDW. On the other hand, as analyzed in [15, 30], weight decay gradually balances radial and perpendicular update components to force the parameter into a pure rotational state. Because of this gradual process, standard optimizers undergo a long *transient phase*. During this early phase, parameter scales and update angles remain unregulated.

Previous works attempt to resolve these issues using heuristic patches, such as dynamic weight decay ratios [14]. In contrast, explicit manifold constraints offer an explicit solution. By restricting the optimization trajectory, our constrained update scheme locks both the relative learning rate  $\eta_{\text{rel},t}$  and the rotation angle  $\theta_t$  exactly from the first iteration, as shown below.

**Locking the Relative Learning Rate.** To analyze the exact dynamics of our optimizer, we formally consider the  $\mathbf{W}$  update step (2) in our algorithm, where the relative learning rate is explicitly locked to a deterministic linear schedule:

$$\eta_{\text{rel},t} = \|\Delta \mathbf{W}_t\|_{\mathcal{M}}/\|\mathbf{W}_t\|_{\mathcal{M}} = \eta_t c R/R = c \eta_t. \quad (4)$$

Our manifold constraint strictly couples the relative update magnitude to the learning rate  $\eta_t$ . This locked  $\eta_{\text{rel},t}$  prevents late-stage gradient amplification under a decaying learning rate schedule. It also enables strict Maximal Update Parametrization ( $\mu\text{P}$ ) transfer. Appendix D.2 provides the empirical verification for the gradient norm decay and the  $\mu\text{P}$  transfer.

**Static Rotational Equilibrium under the Frobenius Sphere.** Manifold constraints also fundamentally alter the angular trajectory. Traditional weight decay requires a transient phase to reach rotational equilibrium [15]. Manifold constraints bypass this phase entirely and enforce a pure rotational state from the very first step.

We explicitly quantify the rotational angle for the Frobenius sphere  $\mathcal{M}_F(R)$ . Define  $\alpha_t := \cos \angle(\mathbf{W}_t, O_t)$ , substituting  $\tilde{\mathbf{V}}_t = (cR/\|O_t\|_F)O_t$  in the update formula we have:

$$\langle \mathbf{W}_t - \eta_t \tilde{\mathbf{V}}_t, \mathbf{W}_t \rangle_F = R^2(1 - \eta_t c \alpha_t), \quad \|\mathbf{W}_t - \eta_t \tilde{\mathbf{V}}_t\|_F = R \sqrt{1 - 2\eta_t c \alpha_t + \eta_t^2 c^2}.$$

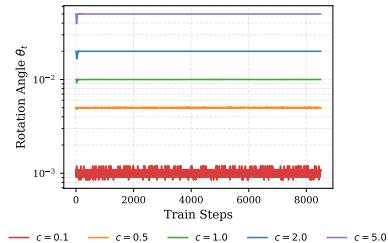


Figure 4:  $\theta_t$  under Frobenius Sphere.

<sup>†</sup>This gap represents the difference in best validation loss between the 330M standard baseline (2.714 in Table 4) and our 330M model without learnable RMSNorm (2.739 in Table 3). Both models are trained with the MACRO-spec optimizer.

Using this inner product constraint, we explicitly compute the rotational angle  $\theta_t$  between consecutive steps:

$$\theta_t = \arccos\left(\frac{\langle \mathbf{W}_{t+1}, \mathbf{W}_t \rangle_F}{\|\mathbf{W}_{t+1}\|_F \|\mathbf{W}_t\|_F}\right) = \arccos\left(\frac{1 - \eta_t c \alpha_t}{\sqrt{1 - 2\eta_t c \alpha_t + \eta_t^2 c^2}}\right)$$

Applying the second-order Taylor expansion for the cosine function, we obtain a simple geometric identity:  $\theta_t \approx \eta_t c \sqrt{1 - \alpha_t^2} \approx \eta_t c$  as  $\alpha_t \approx 0$  (details in Appendix C.3). This indicates that the Frobenius sphere constraint directly enforces a steady-state rotation while standard weight decay penalizes the norm to force a rotation. The full algebraic derivation is in Appendix C.3.

To empirically validate this dynamic, we train a 330M Qwen3-like architecture using a constant learning rate 0.01 and various alignment ratios  $c$  ranging from  $[0.1, 5.0]$ . As Figure 4 shows, the Frobenius rotation angle remains flat, confirming our derived identity  $\theta_t^{\text{fro}} \approx c\eta_t$ .

**Adaptive Rotational Equilibrium under the Spectral Sphere.** We now analyze the rotation angle  $\theta_t$  for spectral sphere, which requires a different approach because spectral norm is not induced by an inner product. Instead of a single global rotation angle, the rotation is anisotropic: different singular subspaces rotate by different amounts. We focus on the maximum singular subspace, which is a natural choice because the spectral sphere explicitly regulates the maximum singular value. Let  $\mathbf{u}_t$  and  $\mathbf{v}_t$  denote the leading left and right singular vectors of  $\mathbf{W}_t$ . We define the effective rotational angle for this primary direction as  $\theta_t = \max\{\theta_u, \theta_v\}$ , where  $\theta_u = \arccos(|\mathbf{u}_{t+1}^\top \mathbf{u}_t|)$  and  $\theta_v = \arccos(|\mathbf{v}_{t+1}^\top \mathbf{v}_t|)$ . We treat our unprojected update step  $-\eta_t \cdot \tilde{\nabla}_t$  as the perturbation matrix, with magnitude  $\|\Delta \mathbf{W}_t\|_2 = \eta_t c R$ . By Wedin sin  $\Theta$  theorem [31, 32], we provide the following bound (see Appendix C.4 for proofs):

$$\max\{\sin \theta_u, \sin \theta_v\} \leq \|\Delta \mathbf{W}_t\|_2 / \Delta_1 \approx \eta_t c R / \Delta_1.$$

Here we assume the leading singular value is unique, so the spectral gap  $\Delta_1 := R - \sigma_2(\mathbf{W}_{t+1}) > 0$ . Substituting this definition into the above bound yields:  $\sin \theta_t \lesssim \frac{\eta_t c R}{R - \sigma_2(\mathbf{W}_{t+1})}$ . Applying the small-angle approximation ( $\sin \theta \approx \theta$ ), we obtain:

$$\theta_t \lesssim \eta_t c \left( \frac{R}{R - \sigma_2(\mathbf{W}_{t+1})} \right). \quad (5)$$

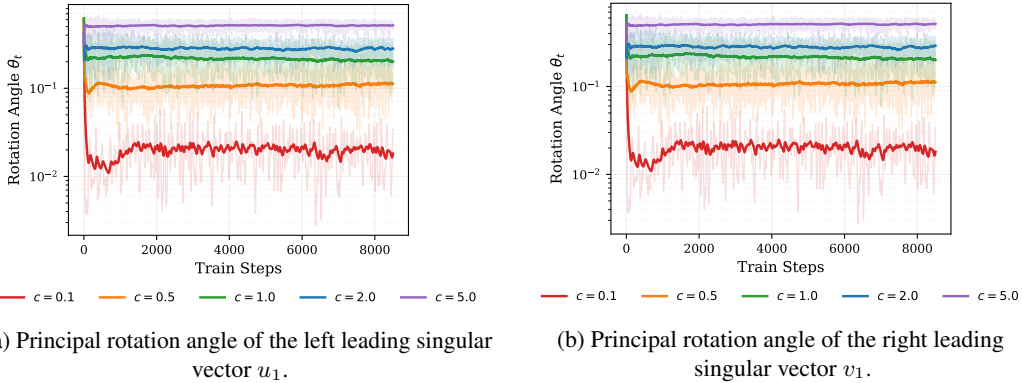


Figure 5: Rotational angle under the spectral constraint: The spectral rotation angles display high-frequency variance. Despite this, both the  $u_1$  and  $v_1$  trajectories remain well-balanced and stable. This dynamic behavior supports our Wedin bound analysis: the local spectral gap continuously modulates these adaptive rotations.

Figure 5 visualizes the principal rotation angles under the spectral constraint. We used the same setting as used in the Frobenius Sphere experiment depicted in Figure 4. Geometrically, the left and right singular vectors  $u_1$  and  $v_1$  rotate the output and input features, respectively. Despite this difference, both subspaces exhibit highly similar rotational trajectories, which indicates that the input and output feature rotations remain well-balanced during training. Furthermore, comparing the rotation angle under the spectral constraint (Eq. (5)) to the Frobenius case ( $\theta_t \approx \eta_t c$ , Figure 4)

reveals a key difference. The Frobenius constraint imposes a static, global rotation determined purely by constant hyperparameters. In contrast, the spectral constraint induces an *adaptive* rotation. For the leading feature dimension, the training-dependent spectral gap  $R - \sigma_2(\mathbf{W}_{t+1})$  explicitly modulates the rotation angle. These distinct behaviors support our theoretical analysis.

🗨️ **Key Takeaway:** (i) *Weight decay is not needed if we use a manifold constraint optimizer.* (ii) *Unlike weight decay, manifold constraints regulate the relative learning rate and rotation angle from the very first iteration; while the Frobenius sphere enforces a static global rotation, the Spectral sphere induces an adaptive, anisotropic rotation.*

## 5 Numerical Justification

To evaluate the empirical performance of MACRO, we train QWEN3-like architectures (ranging from 120M to 1B) equipped with SwiGLU activations, Grouped-Query Attention (GQA), Rotary Positional Embeddings (RoPE), and pre-normalization RMSNorm. Across all model sizes, our token budgets exceed the Chinchilla-optimal token budget. Exact token budgets are detailed in Table 10 in Appendix D.3. We utilize the standard PyTorch implementation of the Muon [18] optimizer<sup>‡</sup>. To provide a comprehensive comparison of different manifold constraints, we extend the Spectral Sphere Optimization (SSO) algorithm and MuonH onto two Frobenius and Spectral Sphere, respectively, resulting FSO and MuonH-spec algorithms (stated in Appendix B.2). Table 4 summarizes the train and test validation losses. Detailed experimental and hyperparameters settings are in Appendix D.3. We draw three conclusions from these results.

Table 4: Train and test validation loss for QWEN3-like models across different parameter scales.

Optimizers	120M		330M		1B	
	Train	Validate	Train	Validate	Train	Validate
Muon (Baseline)	3.008	3.019	2.684	2.736	2.419	2.473
MuonH-fro	2.997	3.007	2.680	2.717	2.404	2.468
MuonH-spec	3.008	3.019	2.679	2.716	2.409	2.464
FSO <sup>†</sup>	<b>2.990</b>	<b>3.001</b>	2.690	2.726	-	-
SSO <sup>†</sup>	3.001	3.011	2.675	<b>2.712</b>	-	-
MACRO-fro (Ours)	2.995	3.005	2.670	2.718	2.403	2.467
MACRO-spec (Ours)	3.007	3.017	<b>2.665</b>	2.714	<b>2.398</b>	<b>2.461</b>

<sup>†</sup> Scaling these double-loop algorithms require custom CUDA kernels. Due to limited computational resources and the absence of such operator-level optimizations, we omit SSO and FSO for the 1B model.

- Manifold constraints consistently improve validation loss across all model scales over the unconstrained baseline. This improvement empirically verifies our analysis in Section 4.3. Specifically, manifold constraints regulate training dynamics more effectively than heuristic weight decay which aligns with the findings in [11].
- The Spectral and Frobenius constraints exhibit similar overall performance. Unlike the normalization-free experiments (Section 4.2), the Spectral constraint provides only marginal improvements over the Frobenius constraint at the 330M and 1B scales. This marginal difference remains consistent across all evaluated optimizers. This similarity occurs because the model’s RMSNorm layers explicitly control activation scales. Consequently, these normalization layers override the distinct activation control mechanisms discussed in Section 4.1.
- Compared to MuonH, MACRO achieves comparable or slightly better performance. Algorithmically, removing the tangent space projection (Line 6 in Algorithm 1) reduces MACRO to MuonH. This similar performance indicates that removing the projection step does not significantly alter the trajectory. However, removing this step breaks Riemannian optimization principles, whereas MACRO strictly follows them. Furthermore, the fast single-loop approximation of MACRO (which avoids the high computational costs of exact double-loop optimizers such as SSO and FSO) does not degrade the validation loss, as confirmed again by Table 4.

<sup>‡</sup><https://docs.pytorch.org/docs/stable/generated/torch.optim.Muon.html>

## 6 Conclusions

In this paper, we demystify the effects of manifold constraints in LLM pre-training. Theoretically, manifold constraints directly bound the forward activation scale, which stabilizes training without requiring learnable RMS normalization layers. Moreover, these constraints explicitly lock the relative learning rate and enforce a stable rotational equilibrium from the first training step. Our MACRO algorithm effectively subsumes the roles of explicit normalization layers and decoupled weight decay. Evaluation of MACRO on standard large-scale LLM architectures demonstrates that applying manifold constraints improves generalization performance compared to unconstrained baselines. Furthermore, MACRO achieves validation losses comparable to, or slightly better than, existing heuristic methods while strictly following Riemannian optimization principles with rigorous convergence guarantees.

## References

- [1] John Zhao. Towards a principled Muon under  $\mu\text{P}$ : Ensuring spectral conditions throughout training, 2026. URL <https://arxiv.org/abs/2601.01306>.
- [2] Xiaowen Jiang, Andrei Semenov, and Sebastian U. Stich. Enhancing LLM training via spectral clipping, 2026. URL <https://arxiv.org/abs/2603.14315>.
- [3] Md Rifat Arefin, Ravid Shwartz-Ziv, Ernie Chang, Chinnadhurai Sankar, Rylan Conway, Aristide Baratin, Adithya Sagar, and Patrick Huber. Learning in transformers under spectral constraints. In *ICLR 2026 Workshop on Geometry-grounded Representation Learning and Generative Modeling*, 2026.
- [4] Yufei Gu and Zeke Xie. Mano: Restriking manifold optimization for LLM training, 2026. URL <https://arxiv.org/abs/2601.23000>.
- [5] Laker Newhouse, R. Preston Hess, Franz Cesista, Andrii Zahorodnii, Jeremy Bernstein, and Phillip Isola. Training transformers with enforced Lipschitz constants, 2025. URL <https://arxiv.org/abs/2507.13338>.
- [6] Tian Xie, Haoming Luo, Haoyu Tang, Yiwen Hu, Jason Klein Liu, Qingnan Ren, Yang Wang, Wayne Xin Zhao, Rui Yan, Bing Su, Chong Luo, and Baining Guo. Controlled LLM training on spectral sphere, 2026. URL <https://arxiv.org/abs/2601.08393>.
- [7] Kaiwei Yang and Lexiao Lai. Manifold constrained steepest descent, 2026. URL <https://arxiv.org/abs/2601.21487>.
- [8] Hadi Mohaghegh Dolatabadi, Thalaisyasingam Ajanthan, Sameera Ramasinghe, Chamin P Hewa Koneputugodage, Shamane Siriwardhana, Violetta Shevchenko, Karol Pajak, James Snewin, Gil Avraham, and Alexander Long. NuMuon: Nuclear-norm-constrained Muon for compressible LLM training, 2026. URL <https://arxiv.org/abs/2603.03597>.
- [9] Jianlin Su. Fastest descent on a manifold: 4. Muon + spectral sphere, Aug 2025. URL <https://spaces.ac.cn/archives/11241>. (In Chinese).
- [10] Jianlin Su. Fastest descent on a manifold: 2. Muon + orthogonal, Aug 2025. URL <https://spaces.ac.cn/archives/11215>. (In Chinese).
- [11] Kaiyue Wen, Xingyu Dang, Kaifeng Lyu, Tengyu Ma, and Percy Liang. Fantastic pretraining optimizers and where to find them 2.1: Hyperball optimization, 12 2025. URL <https://tinyurl.com/muonh>.
- [12] Jeremy Bernstein. Modular manifolds. *Thinking Machines Lab: Connectionism*, 2025. doi: 10.64434/tml.20250926. <https://thinkingmachines.ai/blog/modular-manifolds/>.
- [13] Ilya Loshchilov and Frank Hutter. Decoupled weight decay regularization, 2019. URL <https://arxiv.org/abs/1711.05101>.
- [14] Aaron Defazio. Why gradients rapidly increase near the end of training, 2025. URL <https://arxiv.org/abs/2506.02285>.
- [15] Atli Kosson, Bettina Messmer, and Martin Jaggi. Rotational equilibrium: How weight decay balances learning across neural networks, 2024. URL <https://arxiv.org/abs/2305.17212>.
- [16] Zeke Xie, Zhiqiang Xu, Jingzhao Zhang, Issei Sato, and Masashi Sugiyama. On the overlooked pitfalls of weight decay and how to mitigate them: A gradient-norm perspective, 2024. URL <https://arxiv.org/abs/2011.11152>.
- [17] Francesco D’Angelo, Maksym Andriushchenko, Aditya Varre, and Nicolas Flammarion. Why do we need weight decay in modern deep learning?, 2024. URL <https://arxiv.org/abs/2310.04415>.
- [18] Keller Jordan. Muon: An optimizer for hidden layers, 2024. URL <https://github.com/KellerJordan/Muon>.
- [19] Yossi Arjevani, Yair Carmon, John C Duchi, Dylan J Foster, Nathan Srebro, and Blake Woodworth. Lower bounds for non-convex stochastic optimization. *Mathematical Programming*, 199(1):165–214, 2023.
- [20] Greg Yang, James B Simon, and Jeremy Bernstein. A spectral condition for feature learning. *arXiv preprint arXiv:2310.17813*, 2023.
- [21] Jianlin Su. Beyond MuP: 2. linear layers and steepest descent, Feb 2026. URL <https://spaces.ac.cn/archives/11605>. (In Chinese).

- [22] Zhi-Dong Bai and Yong-Qua Yin. Limit of the smallest eigenvalue of a large dimensional sample covariance matrix. *Ann. Probab.*, 21(3):1275–1294, 1993.
- [23] Sergey Ioffe and Christian Szegedy. Batch normalization: Accelerating deep network training by reducing internal covariate shift, 2015. URL <https://arxiv.org/abs/1502.03167>.
- [24] Yuxin Wu and Kaiming He. Group normalization. In *Proceedings of the European Conference on Computer Vision (ECCV)*, September 2018.
- [25] Jimmy Lei Ba, Jamie Ryan Kiros, and Geoffrey E. Hinton. Layer normalization, 2016. URL <https://arxiv.org/abs/1607.06450>.
- [26] Tim Salimans and Diederik P. Kingma. Weight normalization: A simple reparameterization to accelerate training of deep neural networks, 2016. URL <https://arxiv.org/abs/1602.07868>.
- [27] Siyuan Qiao, Huiyu Wang, Chenxi Liu, Wei Shen, and Alan Yuille. Micro-batch training with batch-channel normalization and weight standardization, 2020. URL <https://arxiv.org/abs/1903.10520>.
- [28] Biao Zhang and Rico Sennrich. Root mean square layer normalization, 2019. URL <https://arxiv.org/abs/1910.07467>.
- [29] Shuo Xie and Zhiyuan Li. Implicit bias of AdamW:  $\ell_\infty$  norm constrained optimization, 2024. URL <https://arxiv.org/abs/2404.04454>.
- [30] Zhiyuan Li, Kaifeng Lyu, and Sanjeev Arora. Reconciling modern deep learning with traditional optimization analyses: The intrinsic learning rate, 2020. URL <https://arxiv.org/abs/2010.02916>.
- [31] Chandler Davis and William Morton Kahan. The rotation of eigenvectors by a perturbation. iii. *SIAM Journal on Numerical Analysis*, 7(1):1–46, 1970.
- [32] Per-Åke Wedin. Perturbation bounds in connection with singular value decomposition. *BIT Numerical Mathematics*, 12(1):99–111, 1972.
- [33] Thomas Pethick, Wanyun Xie, Kimon Antonakopoulos, Zhenyu Zhu, Antonio Silveti-Falls, and Volkan Cevher. Training deep learning models with norm-constrained LMOs, 2025. URL <https://arxiv.org/abs/2502.07529>.
- [34] Runa Eschenhagen, Aaron Defazio, Tsung-Hsien Lee, Richard E. Turner, and Hao-Jun Michael Shi. Purifying Shampoo: Investigating Shampoo’s heuristics by decomposing its preconditioner, 2025. URL <https://arxiv.org/abs/2506.03595>.
- [35] Vineet Gupta, Tomer Koren, and Yoram Singer. Shampoo: Preconditioned stochastic tensor optimization. In *International Conference on Machine Learning*, pages 1842–1850. PMLR, 2018.
- [36] Runa Eschenhagen, Anna Cai, Tsung-Hsien Lee, and Hao-Jun Michael Shi. Clarifying Shampoo: Adapting spectral descent to stochasticity and the parameter trajectory, 2026. URL <https://arxiv.org/abs/2602.09314>.
- [37] Hao-Jun Michael Shi, Tsung-Hsien Lee, Shintaro Iwasaki, Jose Gallego-Posada, Zhijing Li, Kaushik Rangadurai, Dheevatsa Mudigere, and Michael Rabbat. A distributed data-parallel pytorch implementation of the distributed Shampoo optimizer for training neural networks at-scale, 2023. URL <https://arxiv.org/abs/2309.06497>.
- [38] Jeremy Bernstein and Laker Newhouse. Old optimizer, new norm: An anthology. *arXiv preprint arXiv:2409.20325*, 2024.
- [39] Kang An, Yuxing Liu, Rui Pan, Yi Ren, Shiqian Ma, Donald Goldfarb, and Tong Zhang. ASGO: Adaptive structured gradient optimization, 2025. URL <https://arxiv.org/abs/2503.20762>.
- [40] Chao Ma, Wenbo Gong, Meyer Scetbon, and Edward Meeds. SWAN: SGD with normalization and whitening enables stateless LLM training, 2025. URL <https://arxiv.org/abs/2412.13148>.
- [41] Athanasios Glentis, Jiayang Li, Andi Han, and Mingyi Hong. A minimalist optimizer design for LLM pretraining, 2025. URL <https://arxiv.org/abs/2506.16659>.
- [42] Ruihan Xu, Jiajin Li, and Yiping Lu. On the width scaling of neural optimizers under matrix operator norms i: Row/column normalization and hyperparameter transfer, 2026. URL <https://arxiv.org/abs/2603.09952>.

- [43] Meyer Scetbon, Chao Ma, Wenbo Gong, and Edward Meeds. Gradient multi-normalization for stateless and scalable LLM training, 2025. URL <https://arxiv.org/abs/2502.06742>.
- [44] Takeru Miyato, Toshiki Kataoka, Masanori Koyama, and Yuichi Yoshida. Spectral normalization for generative adversarial networks. In *International Conference on Learning Representations*, 2018.
- [45] Yang Liu, Jeremy Bernstein, Markus Meister, and Yisong Yue. Learning by turning: Neural architecture aware optimisation, 2021. URL <https://arxiv.org/abs/2102.07227>.
- [46] Ilya Loshchilov, Cheng-Ping Hsieh, Simeng Sun, and Boris Ginsburg. nGPT: Normalized transformer with representation learning on the hypersphere, 2024. URL <https://arxiv.org/abs/2410.01131>.
- [47] Yonggan Fu, Xin Dong, Shizhe Diao, Matthijs Van keirsbilck, Hanrong Ye, Wonmin Byeon, Yashaswi Karnati, Lucas Liebenwein, Hannah Zhang, Nikolaus Binder, Maksim Khadkevich, Alexander Keller, Jan Kautz, Yingyan Celine Lin, and Pavlo Molchanov. Nemotron-flash: Towards latency-optimal hybrid small language models, 2025. URL <https://arxiv.org/abs/2511.18890>.
- [48] Jörg K.H. Franke, Urs Spiegelhalter, Marianna Nezhurina, Jenia Jitsev, Frank Hutter, and Michael Hefenbrock. Learning in compact spaces with approximately normalized transformer, 2025. URL <https://arxiv.org/abs/2505.22014>.
- [49] Ruosi Wan, Zhanxing Zhu, Xiangyu Zhang, and Jian Sun. Spherical motion dynamics: Learning dynamics of normalized neural network using SGD and weight decay. In M. Ranzato, A. Beygelzimer, Y. Dauphin, P.S. Liang, and J. Wortman Vaughan, editors, *Advances in Neural Information Processing Systems*, volume 34, pages 21759–21770. Curran Associates, Inc., 2021. URL <https://proceedings.neurips.cc/paper/2021/hash/326a8c055c0d04f5b06544665d8bb3ea-Abstract.html>.
- [50] Weiyang Liu, Zhen Liu, Zhiding Yu, Bo Dai, Rongmei Lin, Yisen Wang, James M. Rehg, and Le Song. Decoupled networks. In *Proceedings of the IEEE Conference on Computer Vision and Pattern Recognition*, 2018.
- [51] Takeru Miyato, Sindy Löwe, Andreas Geiger, and Max Welling. Artificial kuramoto oscillatory neurons, 2024. URL <https://arxiv.org/abs/2410.13821>.
- [52] Tero Karras, Miika Aittala, Jaakko Lehtinen, Janne Hellsten, Timo Aila, and Samuli Laine. Analyzing and improving the training dynamics of diffusion models, 2024. URL <https://arxiv.org/abs/2312.02696>.
- [53] Louis Owen, Abhay Kumar, Nilabhra Roy Chowdhury, and Fabian Gürk. Variance control via weight rescaling in LLM pre-training, 2025. URL <https://arxiv.org/abs/2503.17500>.
- [54] Guodong Zhang, Chaoqi Wang, Bowen Xu, and Roger Grosse. Three mechanisms of weight decay regularization, 2018. URL <https://arxiv.org/abs/1810.12281>.
- [55] Zhenxun Zhuang, Mingrui Liu, Ashok Cutkosky, and Francesco Orabona. Understanding AdamW through proximal methods and scale-freeness, 2022. URL <https://arxiv.org/abs/2202.00089>.
- [56] Zhiyuan Li and Sanjeev Arora. An exponential learning rate schedule for deep learning, 2019. URL <https://arxiv.org/abs/1910.07454>.
- [57] Byeongho Heo, Sanghyuk Chun, Seong Joon Oh, Dongyoon Han, Sangdoon Yun, Gyuwan Kim, Youngjung Uh, and Jung-Woo Ha. AdamP: Slowing down the slowdown for momentum optimizers on scale-invariant weights, 2021. URL <https://arxiv.org/abs/2006.08217>.
- [58] Twan van Laarhoven. L2 regularization versus batch and weight normalization, 2017. URL <https://arxiv.org/abs/1706.05350>.
- [59] Atli Kosson, Bettina Messmer, and Martin Jaggi. Analyzing & reducing the need for learning rate warmup in GPT training, 2024. URL <https://arxiv.org/abs/2410.23922>.
- [60] Jianlin Su. Beyond MuP: 4. ensuring parameter stability, Apr 2026. URL <https://spaces.ac.cn/archives/11729>. (In Chinese).
- [61] Lizhang Chen, Bo Liu, Kaizhao Liang, and Qiang Liu. Lion secretly solves constrained optimization: As Lyapunov predicts, 2025. URL <https://arxiv.org/abs/2310.05898>.
- [62] Adrian S Lewis and Hristo S Sendov. Nonsmooth analysis of singular values. part i: Theory. *Set-Valued Analysis*, 13(3):213–241, 2005.

- [63] John M Lee. Smooth manifolds. In *Introduction to smooth manifolds*, pages 1–29. Springer, 2003.
- [64] Roger A. Horn and Charles R. Johnson. *Topics in Matrix Analysis*. Cambridge University Press, 1991.
- [65] Mark Rudelson and Roman Vershynin. Sampling from large matrices: An approach through geometric functional analysis. *Journal of the ACM*, 54(4):21:1–21:19, 2007.
- [66] G. W. Stewart and Ji-Guang Sun. *Matrix Perturbation Theory*. Computer Science and Scientific Computing. Academic Press, 1990.
- [67] Andrej Karpathy. NanoChat: The best ChatGPT that \$100 can buy, 2025. URL <https://github.com/karpathy/nanochat>.

## A Related Works

**Muon optimizers and manifold-constrained variants.** Muon [18, 33] introduced a spectral-norm steepest descent update for weight matrices, achieving strong empirical performance in LLM pre-training. It is a parallel work of matrix structured preconditioning methods such as Shampoo [34–37]. Bernstein and Newhouse [38] provided theoretical grounding by interpreting Muon as an approximate Newton’s method on the Stiefel manifold. Subsequent work has extended Muon in several directions: Zhao [1] ensured spectral conditions under the  $\mu P$  parameterization; An et al. [39] proposed ASGO, which generalizes structured gradient preconditioning across different matrix decompositions; and Dolatabadi et al. [8] introduced NuMuon, which replaces the spectral constraint with a nuclear norm constraint to encourage low-rank structure during training. Some recent studies on structure-aware optimizers [40–43] also consider row/column-wise normalization for the gradient. In parallel, several methods have explored explicit manifold constraints for LLM training. SSO [6] formulates training on the spectral sphere with provable double-loop projections, while Mano [4] targets oblique manifolds and demonstrates competitive pre-training results. MuonH [11] constrains weights to a Frobenius sphere via heuristic normalization after each Muon step. Yang and Lai [7] study Stiefel manifold steepest descent from a general Riemannian optimization perspective.

**Training deep learning models with constraints.** Imposing structural constraints on neural network weights has a long history. Spectral normalization [44] was originally proposed to stabilize GAN training by controlling the Lipschitz constant of discriminator layers. Newhouse et al. [5] extended this idea to enforce Lipschitz bounds in transformers. Pethick et al. [33] trained deep networks with norm-constrained linear minimization oracles (LMOs), offering a Frank-Wolfe perspective on constrained optimization. Liu et al. [45] proposed optimization directly on the Stiefel manifold by decomposing updates into rotations, and Arefin et al. [3] studied spectral constraints for feature learning in transformers. At the architecture level, nGPT [46] normalizes all representations to lie on a hypersphere, and Nemotron-Flash [47] builds on this design for latency-efficient models. Franke et al. [48] further explore approximately normalized transformers that learn in compact parameter spaces. Bernstein [12] provides a conceptual framework connecting modular network design to manifold structure. While these methods each address specific constraint types, none systematically investigates how different manifold geometries interact with normalization layers and weight decay during LLM pre-training.

**Normalization layers and their variants.** Batch Normalization [23] introduced per-channel normalization of activations and was followed by Layer Normalization [25], Group Normalization [24], and RMSNorm [28]. In particular, RMSNorm is now standard in transformer-based LLMs. In the weight space, Weight Normalization [26] decouples the magnitude and direction of weight vectors, and Weight Standardization [27] normalizes the rows of weight matrices to improve micro-batch training. Wan et al. [49] analyze how the combination of batch normalization and weight decay induces spherical motion dynamics, revealing that the effective learning rate is governed by the angular update rather than the Euclidean step size. Liu et al. [50] propose Decoupled Networks, which separate the angular and radial components of inner products in linear layers. Miyato et al. [51] introduce Artificial Kuramoto Oscillatory Neurons, whose phase-based representations naturally reside on the unit circle. Karras et al. [52] demonstrate that weight normalization of convolution layers stabilizes diffusion model training by controlling magnitude growth. Owen et al. [53] propose weight rescaling to control activation variance during LLM pre-training. Our work demonstrates that manifold constraints on weight matrices can formally subsume the stabilizing role of explicit normalization layers, enabling normalization-free linear blocks without sacrificing training stability.

**Weight decay and its dynamics.** Weight decay was originally introduced as  $\ell_2$  regularization to improve generalization [54], and Loshchilov and Hutter [13] showed that decoupling it from the gradient (as in AdamW) leads to substantially different behavior than classical  $\ell_2$  penalties. Zhuang et al. [55] further clarify this distinction through proximal operator interpretations. A key insight from Li et al. [30] is that for scale-invariant

networks, weight decay controls the *intrinsic learning rate*—the ratio of the update norm to the weight norm—rather than acting as a direct regularizer. Li and Arora [56] further show that this mechanism induces an implicit exponential learning rate schedule. Kosson et al. [15] formalize this as *rotational equilibrium*, showing that weight decay balances the angular velocity of weight updates across layers. Heo et al. [57] propose AdamP, which explicitly removes the radial component of momentum updates to prevent the slowdown effect on scale-invariant weights. van Laarhoven [58] analyze the interaction between  $\ell_2$  regularization and batch/weight normalization, showing that their combined effect reduces to a modulation of the effective step size. Kosson et al. [59] connect weight decay dynamics to learning rate warmup, demonstrating that careful weight initialization can reduce the need for warmup in GPT training. Xie et al. [16] identify gradient-norm pathologies caused by weight decay, and D’Angelo et al. [17] revisit why weight decay remains necessary in modern architectures, attributing its benefit primarily to scale invariance. Xu et al. [42], Su [60] and Chen et al. [61] show that weight decay together with bounded update directions keeps the parameters in a uniformly bounded ball. Finally, Defazio [14] show that gradient norms increase rapidly near the end of training, a phenomenon linked to the decay of weight norms. Our analysis shows that manifold constraints intrinsically govern the quantities that weight decay controls heuristically—locking the relative learning rate and rotation angle—and thus provide a principled geometric alternative to weight decay tuning.

## B Algorithm Supplementary Materials

### B.1 Tangent Space Projection and Projectional Retraction

**Tangent Space Projection.** A critical component of our single-loop algorithm is the orthogonal projection of the momentum  $M_t$  (or gradient) onto the tangent space of the constraint manifold. We define the projected vector  $\Phi_t^*$  as the solution to the following proximity problem:

$$\Phi_t^* = \arg \min_{\Phi \in T_{\mathcal{M}} \mathbf{W}_t} \|\Phi - M_t\|_F^2.$$

Given that the constraints we consider can be locally characterized by a scalar function  $h(W) = c$ , the tangent space is a linear subspace. This yields a simple closed-form solution:

$$\Phi_t^* = M_t - \frac{\langle M_t, \Theta \rangle}{\|\Theta\|_F^2} \Theta,$$

where  $\Theta = \nabla_W h(W)$  represents the normal vector to the constraint surface. This projection is highly computationally efficient, as it typically involves only fundamental matrix-vector or inner products. The specific projection operators for our four constraints are detailed below:

- Frobenius Sphere Constraint ( $\mathcal{M}_F$ ): The normal vector is the weight matrix itself,  $\Theta = W$ . The projection is given by:

$$\Phi_t^* = M_t - \frac{\langle M_t, W \rangle}{\|W\|_F^2} W.$$

- Spectral Sphere Constraint ( $\mathcal{M}_S$ ): The normal vector is  $\Theta = u_1 v_1^\top$ , where  $u_1$  and  $v_1$  are the leading singular vectors of weight matrices  $\mathbf{W}$ . Since  $\|\Theta\|_F^2 = \text{Trace}(v_1 u_1^\top u_1 v_1^\top) = 1$ , the projection simplifies to:

$$\Phi_t^* = M_t - \text{Trace}(M_t^\top u_1 v_1^\top) u_1 v_1^\top = M_t - (u_1^\top M_t v_1) u_1 v_1^\top.$$

- Output Oblique Manifold Constraint ( $\mathcal{M}_{O_{\text{out}}}$ ): Since the constraint is applied to each row independently, we project each row vector  $M_t[i, :]$  onto the orthogonal complement of the corresponding weight row  $W_{i,:}$ :

$$\Phi_t^*[i, :] = M_t[i, :] - \frac{M_t[i, :] W_{i,:}^\top}{\|W_{i,:}\|_2^2} W_{i,:}.$$

- Input Oblique Manifold Constraint ( $\mathcal{M}_{O_{\text{in}}}$ ): Symmetrically, the constraint applies to the columns. We project each column vector  $M_t[:, j]$  independently:

$$\Phi_t^*[:, j] = M_t[:, j] - \frac{W_{:,j}^\top M_t[:, j]}{\|W_{:,j}\|_2^2} W_{:,j}.$$

**Projectional Retraction.** The second critical component of our single-loop algorithm is the retraction of the update  $\tilde{\mathbf{W}}_t := \mathbf{W}_t - \eta_t \tilde{\nabla}_t$  to the constraint manifold. Again we use the projectional retraction:

$$\mathbf{W}_{t+1} = \mathcal{P}_{\mathcal{M}}(\tilde{\mathbf{W}}_t) := \arg \min_{\mathbf{W} \in \mathcal{M}} \|\mathbf{W} - \tilde{\mathbf{W}}_t\|_F^2.$$

The specific projectional retraction operators for our four constraints are detailed below:

- Frobenius Sphere Constraint ( $\mathcal{M}_F(R)$ ): The projection is given by:

$$\mathbf{W}_{t+1} = \mathcal{P}_{\mathcal{M}}(\tilde{\mathbf{W}}_t) = R \cdot \tilde{\mathbf{W}}_t / \|\tilde{\mathbf{W}}_t\|_F.$$

- Spectral Sphere Constraint ( $\mathcal{M}_S(R)$ ): The projection is given by:

$$\mathbf{W}_{t+1} = \mathcal{P}_{\mathcal{M}}(\tilde{\mathbf{W}}_t) = U\Sigma'V^\top,$$

where  $U\Sigma V^\top = \tilde{\mathbf{W}}_t$  is the singular value decomposition of  $\tilde{\mathbf{W}}_t$  and  $\Sigma'$  is in the following structure: if  $\Sigma$  has elements that are greater than  $R$ , then clip them to  $R$ ; otherwise if all elements in  $\Sigma$  are smaller than  $R$ , then turn the largest element of  $\Sigma$  to  $R$ . However, this operation is quite expensive to compute in practice, and we use the following approximate operation in all our experiments:

$$\mathbf{W}_{t+1} = R \cdot \tilde{\mathbf{W}}_t / \|\tilde{\mathbf{W}}_t\|_2$$

to approximately project the matrix  $\tilde{\mathbf{W}}_t$  back to the spectral manifold.

- Output Oblique Manifold Constraint ( $\mathcal{M}_{O_{\text{out}}}$ ): Since the constraint is applied to each row independently, the projectional retraction is simply divide each row with its own norm, and multiply with  $R$ .
- Input Oblique Manifold Constraint ( $\mathcal{M}_{O_{\text{in}}}$ ): Symmetrically, the constraint applies to the columns. The projectional retraction is simply divide each column with its own norm, and multiply with  $R$ .

## B.2 Frobenius Sphere Optimization and MuonH-spec

Inspired by [6], we introduce the Frobenius Sphere Optimization by considering the following subproblem:

$$\begin{aligned} \max_{\Phi} \quad & \langle \mathbf{G}, \Phi \rangle \\ \text{s.t.} \quad & \|\Phi\|_2 = 1, \quad \|\mathbf{W} - \eta R \Phi\|_F = \|\mathbf{W}\|_F = R, \end{aligned} \quad (6)$$

where  $\mathbf{G}$  is the stochastic gradient and  $\mathbf{W}$  is the weight matrix. Using the first-order Taylor's expansion of the Frobenius norm, we have:

$$\|\mathbf{W} - \eta R \Phi\|_F = \|\mathbf{W}\|_F - \eta \langle \mathbf{W}, \Phi \rangle + \mathcal{O}(\eta^2).$$

Using the first order approximation, problem (6) reduces to:

$$\max_{\Phi} \langle \mathbf{G}, \Phi \rangle \quad \text{s.t.} \quad \|\Phi\|_2 = 1, \quad \langle \mathbf{W}, \Phi \rangle = 0. \quad (7)$$

To solve Eq. 7, we consider its Lagrangian relaxation:

$$\max_{\Phi} \langle \mathbf{G} + \lambda \mathbf{W}, \Phi \rangle \quad \text{s.t.} \quad \|\Phi\|_2 = 1.$$

Following Theorem A.1 in [6], the closed-form solution to this relaxed problem is:

$$\Phi(\lambda) = \arg \max_{\|\Phi\|_2=1} \langle \mathbf{G} + \lambda \mathbf{W}, \Phi \rangle = \text{msign}(\mathbf{G} + \lambda \mathbf{W}).$$

To satisfy the tangent space feasibility condition in Eq. 7, we require  $\langle \mathbf{W}, \Phi(\lambda^*) \rangle = 0$ . Theorem A.2 in [6] establishes that the multiplier  $\lambda$  is monotonic under the spectral sphere constraint. We show that this monotonicity also holds for the Frobenius sphere constraint:

**Lemma 1.** *The function*

$$h(\lambda) = \langle \mathbf{W}, \Phi(\lambda) \rangle = \langle \mathbf{W}, \text{msign}(\mathbf{G} + \lambda \mathbf{W}) \rangle$$

*is monotonically non-decreasing with respect to  $\lambda$ . Moreover, there exists a root  $\lambda^* \in \mathbb{R}$  such that  $h(\lambda^*) = 0$ , and any such root rigorously satisfies the bound  $|\lambda^*| \leq \frac{2\|\mathbf{G}\|_*}{\|\mathbf{W}\|_*}$ .*

*Proof.* We first prove that  $h(\lambda)$  is a monotonic non-decreasing function. By the Theorem A.1 in [6], we have:

$$\text{msign}(\mathbf{X}) = \operatorname{argmax}_{\|\mathbf{T}\|_2=1} \langle \mathbf{X}, \mathbf{T} \rangle. \quad (8)$$

Consider two arbitrary scalar values  $\lambda_2 > \lambda_1$ . By the definition of  $\Phi(\lambda) = \text{msign}(\mathbf{G} + \lambda \mathbf{W})$  as the precise maximizer of the inner product  $\langle \mathbf{G} + \lambda \mathbf{W}, \cdot \rangle$  over the unit spectral ball, we establish the following two cross-inequalities:

$$\begin{aligned} & \langle \mathbf{G} + \lambda_1 \mathbf{W}, \Phi(\lambda_1) \rangle \geq \langle \mathbf{G} + \lambda_1 \mathbf{W}, \Phi(\lambda_2) \rangle \\ \Rightarrow & \langle \mathbf{G}, \Phi(\lambda_1) \rangle + \lambda_1 \langle \mathbf{W}, \Phi(\lambda_1) \rangle \geq \langle \mathbf{G}, \Phi(\lambda_2) \rangle + \lambda_1 \langle \mathbf{W}, \Phi(\lambda_2) \rangle, \end{aligned} \quad (9)$$

$$\begin{aligned} & \langle \mathbf{G} + \lambda_2 \mathbf{W}, \Phi(\lambda_2) \rangle \geq \langle \mathbf{G} + \lambda_2 \mathbf{W}, \Phi(\lambda_1) \rangle \\ \Rightarrow & \langle \mathbf{G}, \Phi(\lambda_2) \rangle + \lambda_2 \langle \mathbf{W}, \Phi(\lambda_2) \rangle \geq \langle \mathbf{G}, \Phi(\lambda_1) \rangle + \lambda_2 \langle \mathbf{W}, \Phi(\lambda_1) \rangle. \end{aligned} \quad (10)$$

Summing Equation (9) and Equation (10), the cross-terms involving  $\mathbf{G}$  naturally cancel out, allowing us to derive:

$$\begin{aligned} \lambda_1 \langle \mathbf{W}, \Phi(\lambda_1) \rangle + \lambda_2 \langle \mathbf{W}, \Phi(\lambda_2) \rangle &\geq \lambda_1 \langle \mathbf{W}, \Phi(\lambda_2) \rangle + \lambda_2 \langle \mathbf{W}, \Phi(\lambda_1) \rangle \\ \Rightarrow (\lambda_2 - \lambda_1) \langle \mathbf{W}, \Phi(\lambda_2) \rangle &\geq (\lambda_2 - \lambda_1) \langle \mathbf{W}, \Phi(\lambda_1) \rangle. \end{aligned} \quad (11)$$

Given that  $\lambda_2 - \lambda_1 > 0$ , we can divide both sides by  $\lambda_2 - \lambda_1$  to obtain  $\langle \mathbf{W}, \Phi(\lambda_2) \rangle \geq \langle \mathbf{W}, \Phi(\lambda_1) \rangle$ . This algebraically confirms that  $h(\lambda_2) \geq h(\lambda_1)$ , thus  $h(\lambda)$  is strictly monotonic non-decreasing in  $\lambda$ .

We next localize the root  $\lambda^*$ . For any  $\lambda > \frac{2\|\mathbf{G}\|_*}{\|\mathbf{W}\|_*} > 0$  and setting  $\mathbf{T} = \Phi(\lambda) = \text{msign}(\mathbf{G} + \lambda\mathbf{W})$ , the definition in Equation (8) ensures  $\|\mathbf{T}\|_2 \leq 1$ . We have the relation:

$$\lambda h(\lambda) = \lambda \langle \mathbf{W}, \mathbf{T} \rangle = \langle \mathbf{G} + \lambda\mathbf{W}, \mathbf{T} \rangle - \langle \mathbf{G}, \mathbf{T} \rangle. \quad (12)$$

By the duality of norms, the inner product is bounded by  $\langle \mathbf{G}, \mathbf{T} \rangle \leq \|\mathbf{G}\|_* \|\mathbf{T}\|_2 \leq \|\mathbf{G}\|_*$ . Simultaneously, because  $\mathbf{T}$  maximizes the inner product with  $\mathbf{G} + \lambda\mathbf{W}$ , we have  $\langle \mathbf{G} + \lambda\mathbf{W}, \mathbf{T} \rangle = \|\mathbf{G} + \lambda\mathbf{W}\|_*$ . Applying the reverse triangle inequality:

$$\|\mathbf{G} + \lambda\mathbf{W}\|_* \geq \|\lambda\mathbf{W}\|_* - \|\mathbf{G}\|_* = \lambda\|\mathbf{W}\|_* - \|\mathbf{G}\|_* \quad (13)$$

Substituting Equation (13) and the dual norm bound into Equation (12), we derive:

$$\lambda h(\lambda) \geq (\lambda\|\mathbf{W}\|_* - \|\mathbf{G}\|_*) - \|\mathbf{G}\|_* = \lambda\|\mathbf{W}\|_* - 2\|\mathbf{G}\|_*. \quad (14)$$

Since we assumed  $\lambda > \frac{2\|\mathbf{G}\|_*}{\|\mathbf{W}\|_*}$ , it follows that  $\lambda h(\lambda) > 0$ . Because  $\lambda$  is positive, this implies  $h(\lambda) > 0$ . Through symmetrical logical deduction, if  $\lambda < \frac{-2\|\mathbf{G}\|_*}{\|\mathbf{W}\|_*}$ , we obtain  $\lambda h(\lambda) > 0$ , which inherently forces  $h(\lambda) < 0$  since  $\lambda$  is strictly negative.

Because  $h(\lambda)$  represents a monotonically non-decreasing mapping (as established above) that transitions from a negative state at  $\lambda = \frac{-2\|\mathbf{G}\|_*}{\|\mathbf{W}\|_*}$  to a positive state at  $\lambda = \frac{2\|\mathbf{G}\|_*}{\|\mathbf{W}\|_*}$ , the Intermediate Value Property mathematically guarantees the existence of at least one root  $\lambda^*$  satisfying  $h(\lambda^*) = 0$ . Consequently, any valid root must reside within the bounded interval  $[\frac{-2\|\mathbf{G}\|_*}{\|\mathbf{W}\|_*}, \frac{2\|\mathbf{G}\|_*}{\|\mathbf{W}\|_*}]$ , proving  $|\lambda^*| \leq \frac{2\|\mathbf{G}\|_*}{\|\mathbf{W}\|_*}$ .  $\square$

Leveraging Lemma 1, we can solve the subproblem in Eq. 7 via bisection search. This forms the basis of their double-loop algorithms: Frobenius Sphere Optimization (FSO), as summarized in Algorithm 2.

For MuonH, Wen et al. [11] proposed Muon-Hyperball method under Frobenius Sphere based on the update step:

$$\mathbf{W}_{t+1} = \mathcal{P}_{\mathcal{M}}(\mathbf{W}_t - \eta R \cdot \text{Normalize}(\text{msign}(M_t))).$$

According to the projection Retraction we mentioned in B.1 we can get the MuonH-spec using the following update step:

$$\mathbf{W}_{t+1} = \frac{R \cdot (\mathbf{W}_t - \eta c R \text{msign}(M_t))}{\|\mathbf{W}_t - \eta c R \text{msign}(M_t)\|_2}.$$

---

### Algorithm 2 Frobenius Sphere Optimization (FSO)

---

- 1: **Input:** Weights  $\mathbf{W}_t$ , Learning rate  $\eta_t$ , Hyperparameters  $\beta, R, c$
  - 2: **Output:** Updated Weights  $\mathbf{W}_{t+1}$
  - 3: **for**  $t = 0, 1, \dots$  **do**
  - 4:    $G_t = \nabla \ell(\mathbf{W}_t, \xi_t)$
  - 5:    $M_t = \beta M_{t-1} + (1 - \beta) G_t$
  - 6:   Define  $h(\lambda) = \langle \mathbf{W}_t, \text{msign}(M_t + \lambda \mathbf{W}_t) \rangle$
  - 7:    $\lambda_t^* \leftarrow \text{Bisection}(h, \epsilon)$   $\triangleright$  Find the multiplier  $\lambda$
  - 8:    $O_t \leftarrow \text{msign}(M_t + \lambda_t^* \mathbf{W}_t)$   $\triangleright$  Compute the update direction
  - 9:    $\tilde{\mathbf{V}}_t = cR \cdot O_t / (\|O_t\|_F + \epsilon)$   $\triangleright$  Normalization and Scaling
  - 10:    $\mathbf{W}_{t+1} = \mathcal{P}_{\mathcal{M}}(\mathbf{W}_t - \eta_t \cdot \tilde{\mathbf{V}}_t)$   $\triangleright$  Descent Step and Manifold Projection
  - 11: **end for**
-

## C Theoretical Supplementary Materials

### C.1 Proof for Theorem 1

In this subsection we provide theoretical justification of the proposed MACRO algorithm (Algorithm 1). We prove the convergence result in Theorem 1, which holds for Frobenius, input and output Oblique manifolds.<sup>§</sup>

*Proof of Theorem 1.* This proof follows [7]. By Assumption 1 and 2, for any  $\mathbf{W} \in \mathcal{M}$  and  $G$  we have<sup>¶</sup>

$$\mathcal{L} \circ \mathcal{P}_{\mathcal{M}}(\mathbf{W} + G) \leq \mathcal{L}(\mathbf{W}) + \langle \nabla_{\mathcal{M}} \mathcal{L}(\mathbf{W}), G \rangle + \frac{L}{2} \|G\|_F^2, \quad (15)$$

where  $\nabla_{\mathcal{M}}$  denotes the Riemannian gradient. Now from the algorithm we get

$$\begin{aligned} \mathcal{L}(\mathbf{W}_{t+1}) &= \mathcal{L} \circ \mathcal{P}_{\mathcal{M}}(\mathbf{W} - \eta_t \tilde{\nabla}_t) \leq \mathcal{L}(\mathbf{W}_t) - \eta_t \langle \nabla_{\mathcal{M}} \mathcal{L}(\mathbf{W}_t), \tilde{\nabla}_t \rangle + \frac{L\eta_t^2}{2} \|\tilde{\nabla}_t\|_F^2 \\ &= \mathcal{L}(\mathbf{W}_t) - \langle \nabla_{\mathcal{M}} \mathcal{L}(\mathbf{W}_t), \tilde{\nabla}_t \rangle + \frac{c^2 R^2 L \eta_t^2}{2} \left( \frac{\|O_t\|_F}{\|O_t\|_{\mathcal{M}} + \epsilon} \right)^2. \end{aligned}$$

Note that  $\|O_t\|_2 = 1$ , therefore  $1 \leq \|O_t\|_F^2 \leq d$  with  $d := \min\{D_{\text{in}}, D_{\text{out}}\}$ . Moreover, we may assume a uniform bound  $c_0 \|A\|_F \leq \|A\|_{\mathcal{M}} \leq c_1 \|A\|_F$ . Therefore,

$$\mathcal{L}(\mathbf{W}_{t+1}) \leq \mathcal{L}(\mathbf{W}_t) - \tilde{c} \eta_t \langle \nabla_{\mathcal{M}} \mathcal{L}(\mathbf{W}_t), O_t \rangle + \frac{\tilde{c}^2 L \eta_t^2}{2} d^2,$$

where we denote  $\tilde{c} := \frac{cR}{c_0 + \epsilon}$ . Further, we have

$$\begin{aligned} &\mathcal{L}(\mathbf{W}_{t+1}) \\ &\leq \mathcal{L}(\mathbf{W}_t) - \tilde{c} \eta_t \langle \nabla_{\mathcal{M}} \mathcal{L}(\mathbf{W}_t), O_t \rangle + \frac{\tilde{c}^2 L \eta_t^2}{2} d^2 \\ &= \mathcal{L}(\mathbf{W}_t) - \tilde{c} \eta_t (\langle \nabla_{\mathcal{M}} \mathcal{L}(\mathbf{W}_t) - \text{proj}_{\mathcal{T}_{\mathcal{M}} \mathbf{W}_t}(M_t), O_t \rangle + \langle \text{proj}_{\mathcal{T}_{\mathcal{M}} \mathbf{W}_t}(M_t), O_t \rangle) + \frac{\tilde{c}^2 L \eta_t^2}{2} d. \end{aligned}$$

Since  $O_t = \text{msign}(\Phi_t)$  with  $\Phi_t = \text{proj}_{\mathcal{T}_{\mathcal{M}} \mathbf{W}_t}(M_t)$ , we know that  $\langle \text{proj}_{\mathcal{T}_{\mathcal{M}} \mathbf{W}_t}(M_t), O_t \rangle = \|\Phi_t\|_*$ , therefore (Denote the dual norm of  $\|\cdot\|_{\mathcal{M}}$  as  $\|\cdot\|_{*,\mathcal{M}}$ )

$$\begin{aligned} &\mathcal{L}(\mathbf{W}_{t+1}) \\ &\leq \mathcal{L}(\mathbf{W}_t) + \tilde{c} \eta_t \|\nabla_{\mathcal{M}} \mathcal{L}(\mathbf{W}_t) - \text{proj}_{\mathcal{T}_{\mathcal{M}} \mathbf{W}_t}(M_t)\|_* - \tilde{c} \eta_t \|\Phi_t\|_* + \frac{\tilde{c}^2 L \eta_t^2}{2} d. \end{aligned}$$

By Triangle inequality,  $-\|\Phi_t\|_* \leq -\|\nabla_{\mathcal{M}} \mathcal{L}(\mathbf{W}_t)\|_* + \|\nabla_{\mathcal{M}} \mathcal{L}(\mathbf{W}_t) - \text{proj}_{\mathcal{T}_{\mathcal{M}} \mathbf{W}_t}(M_t)\|_*$ , we have

$$\begin{aligned} &\mathcal{L}(\mathbf{W}_{t+1}) \\ &\leq \mathcal{L}(\mathbf{W}_t) + \tilde{c} \eta_t \|\nabla_{\mathcal{M}} \mathcal{L}(\mathbf{W}_t) - \text{proj}_{\mathcal{T}_{\mathcal{M}} \mathbf{W}_t}(M_t)\|_* - \tilde{c} \eta_t \|\nabla_{\mathcal{M}} \mathcal{L}(\mathbf{W}_t)\|_* + \frac{\tilde{c}^2 L \eta_t^2}{2} d, \end{aligned}$$

i.e.,

$$\begin{aligned} &\tilde{c} \eta_t \|\nabla_{\mathcal{M}} \mathcal{L}(\mathbf{W}_t)\|_* \\ &\leq (\mathcal{L}(\mathbf{W}_t) - \mathcal{L}(\mathbf{W}_{t+1})) + \tilde{c} \eta_t \|\nabla_{\mathcal{M}} \mathcal{L}(\mathbf{W}_t) - \text{proj}_{\mathcal{T}_{\mathcal{M}} \mathbf{W}_t}(M_t)\|_* + \frac{\tilde{c}^2 L \eta_t^2}{2} d. \end{aligned} \quad (16)$$

It remains to bound  $\|\nabla_{\mathcal{M}} \mathcal{L}(\mathbf{W}_t) - \text{proj}_{\mathcal{T}_{\mathcal{M}} \mathbf{W}_t}(M_t)\|_*$ . Since  $\nabla_{\mathcal{M}} \mathcal{L}(\mathbf{W}_t) = \text{proj}_{\mathcal{T}_{\mathcal{M}} \mathbf{W}_t}(\nabla \mathcal{L}(\mathbf{W}_t))$ , we have

$$\begin{aligned} &\|\nabla_{\mathcal{M}} \mathcal{L}(\mathbf{W}_t) - \text{proj}_{\mathcal{T}_{\mathcal{M}} \mathbf{W}_t}(M_t)\|_* = \|\text{proj}_{\mathcal{T}_{\mathcal{M}} \mathbf{W}_t}(\nabla \mathcal{L}(\mathbf{W}_t) - M_t)\|_* \\ &\leq \sqrt{d} \|\text{proj}_{\mathcal{T}_{\mathcal{M}} \mathbf{W}_t}(\nabla \mathcal{L}(\mathbf{W}_t) - M_t)\|_F \quad (\text{WLOG assume full-rankness}) \\ &\leq \sqrt{d} \|\nabla \mathcal{L}(\mathbf{W}_t) - M_t\|_F. \end{aligned}$$

Hence, we just need to bound  $\|\nabla \mathcal{L}(\mathbf{W}_t) - M_t\|_F$ . Denote  $C_t := \beta C_{t-1} + (1 - \beta) \nabla \mathcal{L}(\mathbf{W}_t)$  with  $C_0 := \mathcal{L}(\mathbf{W}_0)$ , we have:

$$\|\nabla \mathcal{L}(\mathbf{W}_t) - M_t\|_F \leq \|\nabla \mathcal{L}(\mathbf{W}_t) - C_t\|_F + \|C_t - M_t\|_F.$$

<sup>§</sup>The analysis follows Yang and Lai [7] for Stiefel manifold. We also point out that the theoretical analysis in [4] explicitly assumes that the angles between the weights and the stochastic gradients are bounded away from zero, which is a very restrictive and non-verifiable assumption.

<sup>¶</sup>Note that we do not require  $G$  to be on the tangent space, as proved in Yang and Lai [7, Lemma 4.4]

For the first term, we have

$$\begin{aligned}
& \|\nabla\mathcal{L}(\mathbf{W}_t) - C_t\|_F \\
&= \|\nabla\mathcal{L}(\mathbf{W}_t) - (\beta C_{t-1} + (1-\beta)\nabla\mathcal{L}(\mathbf{W}_t))\|_F \\
&= \beta\|\nabla\mathcal{L}(\mathbf{W}_t) - C_{t-1}\|_F \\
&\leq \beta\|\nabla\mathcal{L}(\mathbf{W}_t) - \nabla\mathcal{L}(\mathbf{W}_{t-1})\|_F + \beta\|\nabla\mathcal{L}(\mathbf{W}_{t-1}) - C_{t-1}\|_F \\
&\leq \beta L\|\mathbf{W}_t - \mathbf{W}_{t-1}\|_F + \beta\|\nabla\mathcal{L}(\mathbf{W}_{t-1}) - C_{t-1}\|_F \\
&\leq \beta L\eta_t \tilde{c} + \beta\|\nabla\mathcal{L}(\mathbf{W}_{t-1}) - C_{t-1}\|_F.
\end{aligned}$$

Applying recursively we get

$$\|\nabla\mathcal{L}(\mathbf{W}_t) - C_t\|_F \leq L\eta_t \tilde{c} \sum_{i=0}^{t-1} \beta^i \leq \frac{2L\eta_t \tilde{c}}{1-\beta}.$$

For the second term  $\|C_t - M_t\|_F$ , we have

$$\begin{aligned}
& \mathbb{E}\|C_t - M_t\|_F \\
&\leq (1-\beta)\mathbb{E}\left\|\sum_{i=1}^t \beta^{t-i}(G_i - \nabla\mathcal{L}(\mathbf{W}_i))\right\|_F + \beta^t\mathbb{E}\|G_0 - \nabla\mathcal{L}(\mathbf{W}_0)\|_F \\
&\leq (1-\beta)\sqrt{\mathbb{E}\left\|\sum_{i=1}^t \beta^{t-i}(G_i - \nabla\mathcal{L}(\mathbf{W}_i))\right\|_F^2} + \beta^t\sqrt{\mathbb{E}\|G_0 - \nabla\mathcal{L}(\mathbf{W}_0)\|_F^2} \\
&\leq (1-\beta)\sqrt{\sum_{i=1}^t \beta^{2(t-i)}\sigma^2} + \beta^t\sigma \leq \left(\sqrt{\frac{1-\beta}{1+\beta}} + \beta^t\right)\sigma.
\end{aligned}$$

Now plug in everything back to (16), we get

$$\begin{aligned}
& \tilde{c}\eta_t\mathbb{E}\|\nabla_{\mathcal{M}}\mathcal{L}(\mathbf{W}_t)\|_* \\
&\leq \mathbb{E}(\mathcal{L}(\mathbf{W}_t) - \mathcal{L}(\mathbf{W}_{t+1})) + \tilde{c}\eta_t\sqrt{d}\mathbb{E}\|\nabla_{\mathcal{M}}\mathcal{L}(\mathbf{W}_t) - \text{proj}_{T_{\mathcal{M}}\mathbf{W}_t}(M_t)\|_F + \frac{\tilde{c}^2 L\eta_t^2}{2}d \\
&\leq \mathbb{E}(\mathcal{L}(\mathbf{W}_t) - \mathcal{L}(\mathbf{W}_{t+1})) + \tilde{c}(c_0 + 1)\eta_t\sqrt{d}\left(\frac{2L\eta_t\tilde{c}}{1-\beta} + \left(\sqrt{\frac{1-\beta}{1+\beta}} + \beta^t\right)\sigma\right) + \frac{\tilde{c}^2 L\eta_t^2}{2}d.
\end{aligned}$$

Summing up the above inequality from  $t = 0$  to  $T - 1$ , we get

$$\sum_{t=0}^{T-1} \tilde{c}\eta_t\mathbb{E}\|\nabla_{\mathcal{M}}\mathcal{L}(\mathbf{W}_t)\|_* \lesssim \mathbb{E}[\mathcal{L}(\mathbf{W}_0) - \mathcal{L}^*] + \tilde{c}\sqrt{d}\sum_{t=0}^{T-1}\left(\frac{2\beta L\eta_t}{1-\beta} + \left(\sqrt{\frac{1-\beta}{1+\beta}} + \beta^t\right)\sigma\right)\eta_t + \frac{\tilde{c}^2 dL}{2}\sum_{t=0}^{T-1}\eta_t^2.$$

The final result is obtained by plugging in

$$\beta = 1 - \frac{1}{\sqrt{T}}, \quad \eta_t = \eta = \Omega\left(\sqrt{\frac{\Delta}{LT^{3/2}}}\right)$$

to the above inequality.  $\square$

**Discussion on the spectral sphere.** The constraint  $\mathcal{M}_S(R) = \{\mathbf{W} \in \mathbb{R}^{D_{\text{out}} \times D_{\text{in}}} : \|\mathbf{W}\|_2 = R > 0\}$  is actually not a manifold, due to the possible existence of multiple top singular values. This can be proved by the fact that the largest singular value is differentiable only at matrices where it is simple; see Lewis and Soudry [62].

If we restrict the constraint to the subset where the top singular value is unique (and the first and second singular values have a small gap)

$$\tilde{\mathcal{M}}_S(R) = \{\mathbf{W} : \|\mathbf{W}\|_2 = R, \sigma_1(\mathbf{W}) \geq \sigma_2(\mathbf{W}) + \epsilon\}$$

then  $\tilde{\mathcal{M}}_S(R)$  is shown to be a smooth embedded compact submanifold. A simple argument is that, on the closed set  $\Omega = \{X : \sigma_1(X) \geq \sigma_2(X) + \epsilon\}$ , the largest singular value  $X \rightarrow \sigma_1(X)$  is Fréchet differentiable; again see Lewis and Soudry [62]. Also the spectral sphere constraint  $\mathcal{M}_S(R) = \{\mathbf{W} \in \mathbb{R}^{D_{\text{out}} \times D_{\text{in}}} : \|\mathbf{W}\|_2 = R > 0\}$  is a regular level set, therefore their intersection is a smooth embedded submanifold by regular level set theorem; see Lee [63]. We can naturally consider this submanifold to apply Algorithm 1 and conduct a convergence analysis exactly the same as Theorem 1, due to the following reasons.

- The projection onto the tangent space of  $\tilde{\mathcal{M}}_S(R)$  is exactly defined in Appendix B.1;

- It is hard globally compute the projectional retraction onto the set  $\tilde{\mathcal{M}}_S(R)$  (The msign projection may not necessarily keep the top singular value unique). However we argue that this is not a problem in practice: due to stochasticity, the gradients  $G_t$  and  $\Phi_t$  and the updates have unique top singular values with probability one, and msign could serve as the approximate projection in practice.

Therefore, despite the fact that  $\mathcal{M}_S(R)$  is not a smooth manifold, the proposed Algorithm 1 and the convergence analysis in Theorem 1 can be applied for the spectral sphere constraint **as a manifold** almost surely.

## C.2 Theoretical Supplementary Material in Activation Controls in Section 4.1

This appendix provides the full proofs of the two activation-control lemmas underlying Proposition 1, formalizes the oblique-manifold variants discussed in the main body, and reconciles our radius choices with prior work [6, 11, 20].

### C.2.1 Setup: Kronecker Reformulation and the Activation Control Setting

Consider a single linear layer

$$\mathbf{Y} = \mathbf{X}\mathbf{W}^\top, \quad \mathbf{X} \in \mathcal{R}^{T \times D_{\text{in}}}, \mathbf{W} \in \mathcal{R}^{D_{\text{out}} \times D_{\text{in}}}, \mathbf{Y} \in \mathcal{R}^{T \times D_{\text{out}}}, \quad (17)$$

where  $T$  is the sequence length. Whereas earlier theoretical analyses treat the layer output as a single vector, in modern LLMs both  $\mathbf{X}$  and  $\mathbf{Y}$  are matrices. Vectorizing along the sequence dimension yields the equivalent matrix–vector form

$$\text{vec}(\mathbf{Y}) = (\mathbf{W} \otimes \mathbf{I}_T) \text{vec}(\mathbf{X}), \quad (18)$$

with  $\text{vec}(\mathbf{X}) \in \mathcal{R}^{TD_{\text{in}}}$ ,  $\text{vec}(\mathbf{Y}) \in \mathcal{R}^{TD_{\text{out}}}$ , and  $\mathbf{I}_T$  the  $T \times T$  identity matrix. We work throughout with the input scale assumption

$$\|\text{vec}(\mathbf{X})\|_{\text{RMS}} = \Theta(1), \quad (19)$$

and we adopt the activation-control goal of Yang et al. [20]:

$$\boxed{\|\text{vec}(\mathbf{Y})\|_{\text{RMS}} = \Theta(1)}. \quad (20)$$

The factorization (18) exhibits a sharp asymmetry between the spectral and Frobenius norms of the lifted operator  $\mathbf{W} \otimes \mathbf{I}_T$ :

**Lemma 2** (Norms of  $\mathbf{W} \otimes \mathbf{I}_T$ ). *For any  $\mathbf{W} \in \mathcal{R}^{D_{\text{out}} \times D_{\text{in}}}$  and any  $T \geq 1$ ,*

$$\|\mathbf{W} \otimes \mathbf{I}_T\|_2 = \|\mathbf{W}\|_2, \quad \|\mathbf{W} \otimes \mathbf{I}_T\|_F = \sqrt{T} \|\mathbf{W}\|_F. \quad (21)$$

*Proof.* Both identities are standard properties of the Kronecker product: for any matrices  $A, B$ ,  $\|A \otimes B\|_2 = \|A\|_2 \|B\|_2$  and  $\|A \otimes B\|_F = \|A\|_F \|B\|_F$  (see, e.g., 64, §4.2). Substituting  $A = \mathbf{I}_T$  (which has  $\|\mathbf{I}_T\|_2 = 1$  and  $\|\mathbf{I}_T\|_F = \sqrt{T}$ ) and  $B = \mathbf{W}^\top$  proves the claim.  $\square$

The spectral norm is therefore invariant to the sequence length  $T$ , while the Frobenius norm is amplified by a factor of  $\sqrt{T}$ . Consequently the two constraints lead to qualitatively different activation-control mechanisms, treated separately in Appendix C.2.2 and Appendix C.2.3.

### C.2.2 Spectral Sphere: Worst-Case Activation Control

For the spectral case, Lemma 2 immediately reduces the activation analysis to the spectral norm of  $\mathbf{W}$ . The upper bound is straightforward; the matching lower bound requires that  $\mathbf{W}$  remain non-degenerate during training, which we encode in the following assumption.

**Assumption 3** (Anti-rank-collapse for  $\mathbf{W}$ ). *The weight matrix  $\mathbf{W}$  is full rank with probability one throughout training, i.e. all  $\min\{D_{\text{in}}, D_{\text{out}}\}$  singular values of  $\mathbf{W}$  are strictly positive.*

This assumption is well supported in modern LLM pre-training: (i) at initialization, standard Gaussian schemes produce a full-rank matrix almost surely [22]; (ii) during training, the next-token prediction objective penalizes representational collapse, since a low-rank  $\mathbf{W}$  would force a degenerate output distribution and an immediate spike in the training loss. We provide empirical evidence for the persistence of this property in Figure 2.

**Lemma 3** (Spectral activation control). *Under the input scale condition (19) and Assumption 3, if*

$$\|\mathbf{W}\|_2 = \Theta\left(\sqrt{\frac{D_{\text{out}}}{D_{\text{in}}}}\right) \text{ and } \sigma_{\min}(\mathbf{W}) = \Omega(1), \quad (22)$$

*then  $\|\text{vec}(\mathbf{Y})\|_{\text{RMS}} = \Theta(1)$ . Equivalently, the goal (20) is satisfied on the spectral sphere*

$$\mathcal{C}_{\text{spec}}(R_{\text{spec}}) = \left\{ \mathbf{W} \in \mathcal{R}^{D_{\text{out}} \times D_{\text{in}}} \mid \|\mathbf{W}\|_2 = R_{\text{spec}} = \Theta\left(\sqrt{\frac{D_{\text{out}}}{D_{\text{in}}}}\right) \right\}. \quad (23)$$

*Proof. Upper bound.* By Lemma 2 and the operator-norm inequality applied to (18),

$$\|\text{vec}(\mathbf{Y})\|_2 \leq \|\mathbf{W} \otimes I_T\|_2 \|\text{vec}(\mathbf{X})\|_2 = \|\mathbf{W}\|_2 \|\text{vec}(\mathbf{X})\|_2. \quad (24)$$

Dividing both sides by  $\sqrt{TD_{\text{out}}}$  and using  $\|\text{vec}(\mathbf{X})\|_{\text{RMS}} = \|\text{vec}(\mathbf{X})\|_2/\sqrt{TD_{\text{in}}}$ ,

$$\|\text{vec}(\mathbf{Y})\|_{\text{RMS}} \leq \sqrt{\frac{D_{\text{in}}}{D_{\text{out}}}} \|\mathbf{W}\|_2 \|\text{vec}(\mathbf{X})\|_{\text{RMS}} = \mathcal{O}(1), \quad (25)$$

where the last equality uses  $\|\mathbf{W}\|_2 = \Theta(\sqrt{D_{\text{out}}/D_{\text{in}}})$  and (19).

**Lower bound.** Since  $\mathbf{W} \otimes I_T$  has the smallest singular value  $\sigma_{\min}(\mathbf{W})$  (Kronecker product with the identity preserves the singular spectrum up to multiplicity), we have

$$\|\text{vec}(\mathbf{Y})\|_2 \geq \sigma_{\min}(\mathbf{W}) \|\text{vec}(\mathbf{X})\|_2. \quad (26)$$

Under  $\sigma_{\min} = \Omega(1)$  assumption, it yields  $\|\text{vec}(\mathbf{Y})\|_{\text{RMS}} = \Omega(1)$ . Combining the two bounds gives  $\Theta(1)$ .  $\square$

**Remark 1.** *The upper bound in Lemma 3 controls the worst-case singular-value amplification and is therefore tight even for adversarial inputs. The matching lower bound is the geometric content of Assumption 3: without it, the spectral constraint only guarantees  $\|\text{vec}(\mathbf{Y})\|_{\text{RMS}} = \mathcal{O}(1)$ , not  $\Theta(1)$ .*

### C.2.3 Frobenius Sphere: Average-Case Activation Control

The Frobenius sphere is a strictly weaker geometric constraint than the spectral sphere, and the worst-case argument used for Lemma 3 no longer yields a useful radius. We first show why the worst-case bound is uninformative, then derive the correct radius from an average-case analysis.

**Why the worst-case Frobenius bound is uninformative.** Applying the sub-multiplicativity of the Frobenius norm naively gives

$$\|\mathbf{Y}\|_F \leq \|\mathbf{X}\|_F \|\mathbf{W}\|_F, \quad (27)$$

and hence

$$\|\text{vec}(\mathbf{Y})\|_{\text{RMS}} \leq \sqrt{\frac{D_{\text{in}}}{D_{\text{out}}}} \|\mathbf{W}\|_F \|\text{vec}(\mathbf{X})\|_{\text{RMS}}. \quad (28)$$

Forcing the right-hand side to  $\Theta(1)$  would require  $\|\mathbf{W}\|_F = \Theta(\sqrt{D_{\text{out}}/D_{\text{in}}})$ , which is the *same* radius as the spectral sphere. Two observations show this is an empty conclusion. First, equality in  $\|\mathbf{Y}\|_F^2 = \|\mathbf{X}\|_F^2 \|\mathbf{W}\|_F^2$  requires that every row of  $\mathbf{X}$  be collinear with every row of  $\mathbf{W}$  — a representational collapse never observed in real LLM training. Second, at Gaussian initialization  $\mathbf{W}_{ij} \sim \mathcal{N}(0, \sigma^2)$ , the asymptotic regime  $D_{\text{out}}, D_{\text{in}} \rightarrow \infty$  with fixed ratio yields, by Theorem 2 of Bai and Yin [22],

$$\|\mathbf{W}\|_2 \rightarrow \sigma(\sqrt{D_{\text{out}}} + \sqrt{D_{\text{in}}}) \quad \text{a.s.} \quad (29)$$

together with  $\mathbb{E}\|\mathbf{W}\|_F = \sigma\sqrt{D_{\text{in}}D_{\text{out}}}$ , so that

$$\frac{\|\mathbf{W}\|_F}{\|\mathbf{W}\|_2} \rightarrow \frac{\sqrt{D_{\text{in}}D_{\text{out}}}}{\sqrt{D_{\text{out}}} + \sqrt{D_{\text{in}}}} = \frac{\sqrt{D_{\text{out}}}}{1 + \sqrt{D_{\text{out}}/D_{\text{in}}}}. \quad (30)$$

Setting  $\|\mathbf{W}\|_F = \Theta(\sqrt{D_{\text{out}}/D_{\text{in}}})$  would then force  $\|\mathbf{W}\|_2 = \Theta(1/\sqrt{D_{\text{in}}})$ , suppressing the effective gain of the layer by a factor of  $1/\sqrt{D_{\text{out}}}$  and causing severe forward attenuation. The worst-case bound is therefore vacuous for the Frobenius sphere.

**Average-case analysis at initialization.** At initialization the rows  $x_i$  of  $\mathbf{X}$  are well modelled as zero-mean isotropic random vectors with  $\mathbb{E}[x_i x_i^\top] = \sigma_x^2 \mathbf{I}_{D_{\text{in}}}$ . A direct expansion gives

$$\mathbb{E}[\|\mathbf{Y}\|_F^2] = \mathbb{E}[\text{Trace}(\mathbf{X}\mathbf{W}^\top \mathbf{W}\mathbf{X}^\top)] = \text{Trace}\left(\sum_{i=1}^T \mathbb{E}[x_i x_i^\top] \mathbf{W}^\top \mathbf{W}\right) = T \sigma_x^2 \|\mathbf{W}\|_F^2. \quad (31)$$

Hence

$$\mathbb{E}[\|\text{vec}(\mathbf{Y})\|_{\text{RMS}}] = \sqrt{\frac{\mathbb{E}\|\mathbf{Y}\|_F^2}{TD_{\text{out}}}} = \frac{\sigma_x}{\sqrt{D_{\text{out}}}} \|\mathbf{W}\|_F, \quad (32)$$

so that securing  $\Theta(1)$  output scale at initialization requires  $\|\mathbf{W}\|_F = \Theta(\sqrt{D_{\text{out}}}/\sigma_x) = \Theta(\sqrt{D_{\text{out}}})$  when  $\sigma_x = \Theta(1)$ .

**Beyond initialization: covariance and stable rank.** During training, optimization dynamics break isotropy and the input covariance spectrum becomes skewed. We work with the empirical covariance  $\Sigma_{\mathbf{X}} = \frac{1}{T} \mathbf{X}^\top \mathbf{X} \in \mathcal{R}^{D_{\text{in}} \times D_{\text{in}}}$ , which under (19) satisfies

$$\text{Trace}(\Sigma_{\mathbf{X}}) = D_{\text{in}} \cdot \Theta(1). \quad (33)$$

We additionally assume that  $\mathbf{W}$  is well conditioned in the sense of stable rank, a quantitative refinement of Assumption 3 introduced by Rudelson and Vershynin [65].

**Assumption 4** (Stable rank of  $\mathbf{W}$ ). *There exists a constant  $\kappa = \Theta(1)$  such that*

$$\|\mathbf{W}\|_2^2 \leq \frac{\kappa}{\min\{D_{\text{in}}, D_{\text{out}}\}} \|\mathbf{W}\|_F^2. \quad (34)$$

Equivalently, the stable rank  $\text{srk}(\mathbf{W}) := \|\mathbf{W}\|_F^2 / \|\mathbf{W}\|_2^2$  satisfies  $\text{srk}(\mathbf{W}) \geq \min\{D_{\text{in}}, D_{\text{out}}\} / \kappa$ .

We verify Assumption 4 empirically across attention and FFN modules of a trained LLM in Figure 2 of the main body. We can now state and prove the Frobenius counterpart of Lemma 3.

**Lemma 4** (Frobenius activation control). *Under the input scale condition (19), Assumption 3, and the standard Transformer dimension scaling  $D_{\text{in}} / \min\{D_{\text{in}}, D_{\text{out}}\} = \Theta(1)$ , if*

$$\|\mathbf{W}\|_F = \Theta(\sqrt{D_{\text{out}}}), \text{ and } \lambda_{\min}(\Sigma_{\mathbf{X}}) = \Omega(1) \text{ almost surely} \quad (35)$$

then  $\|\text{vec}(\mathbf{Y})\|_{\text{RMS}} = \Theta(1)$ . Equivalently, the goal (20) is satisfied on the Frobenius sphere

$$\mathcal{C}_{\text{fro}}(R_{\text{fro}}) = \left\{ \mathbf{W} \in \mathcal{R}^{D_{\text{out}} \times D_{\text{in}}} \mid \|\mathbf{W}\|_F = R_{\text{fro}} = \Theta(\sqrt{D_{\text{out}}}) \right\}. \quad (36)$$

*Proof.* The expected output energy can be written as

$$\mathbb{E}_{\mathbf{X}} [\|\mathbf{Y}\|_F^2] = T \text{Trace}(\Sigma_{\mathbf{X}} \mathbf{W}^\top \mathbf{W}). \quad (37)$$

**Upper bound.** For positive semidefinite  $A, B$ ,  $\text{Trace}(AB) \leq \text{Trace}(A) \|B\|_2$ , so

$$\text{Trace}(\Sigma_{\mathbf{X}} \mathbf{W}^\top \mathbf{W}) \leq \text{Trace}(\Sigma_{\mathbf{X}}) \|\mathbf{W}\|_2^2 \stackrel{(33),(34)}{\leq} (D_{\text{in}} \cdot \Theta(1)) \cdot \frac{\kappa}{\min\{D_{\text{in}}, D_{\text{out}}\}} \|\mathbf{W}\|_F^2 = \Theta(1) \|\mathbf{W}\|_F^2, \quad (38)$$

where the equality uses  $D_{\text{in}} / \min\{D_{\text{in}}, D_{\text{out}}\} = \max\{1, D_{\text{in}}/D_{\text{out}}\} = \Theta(1)$  for standard Transformer block shapes (e.g.  $D_{\text{in}} = D_{\text{out}}$  in attention projections and  $D_{\text{out}} = 4D_{\text{in}}$  in FFN up-projections). Renormalizing,

$$\mathbb{E}_{\mathbf{X}} [\|\text{vec}(\mathbf{Y})\|_{\text{RMS}}^2] = \frac{\text{Trace}(\Sigma_{\mathbf{X}} \mathbf{W}^\top \mathbf{W})}{D_{\text{out}}} \leq \mathcal{O}\left(\frac{1}{D_{\text{out}}} \|\mathbf{W}\|_F^2\right), \quad (39)$$

so that  $\mathbb{E}_{\mathbf{X}} [\|\text{vec}(\mathbf{Y})\|_{\text{RMS}}] = \mathcal{O}(\|\mathbf{W}\|_F / \sqrt{D_{\text{out}}})$ .

**Lower bound.** For positive semidefinite  $A$  and  $B \succeq 0$ ,  $\text{Trace}(AB) \geq \lambda_{\min}(A) \text{Trace}(B)$ , hence

$$\text{Trace}(\Sigma_{\mathbf{X}} \mathbf{W}^\top \mathbf{W}) \geq \lambda_{\min}(\Sigma_{\mathbf{X}}) \|\mathbf{W}\|_F^2. \quad (40)$$

In typical LLM pre-training the context length  $T$  exceeds the hidden dimension  $D_{\text{in}}$ , so  $\Sigma_{\mathbf{X}} = \frac{1}{T} \mathbf{X}^\top \mathbf{X}$  is full rank and, by (33) together with the absence of dimensional collapse. We also assume  $\sqrt{\lambda_{\min}(\Sigma_{\mathbf{X}})} = \Omega(1)$  almost surely. For every realization of  $\mathbf{X}$  we have,

$$\|\mathbf{Y}\|_F^2 \geq T \lambda_{\min}(\Sigma_{\mathbf{X}}) \|\mathbf{W}\|_F^2 \implies \|\mathbf{Y}\|_F \geq \sqrt{T \lambda_{\min}(\Sigma_{\mathbf{X}})} \|\mathbf{W}\|_F$$

Since  $\Sigma_{\mathbf{X}} \succeq 0$ ,  $\lambda_{\min}(\Sigma_{\mathbf{X}}) = \Omega(1)$  almost surely also gives  $\sqrt{\lambda_{\min}(\Sigma_{\mathbf{X}})} = \Omega(1)$  almost surely. Substituting,

$$\|\text{vec}(\mathbf{Y})\|_{\text{RMS}} \geq \Omega\left(\frac{1}{\sqrt{D_{\text{out}}}} \|\mathbf{W}\|_F\right), \quad (41)$$

so  $\mathbb{E}_{\mathbf{X}} [\|\text{vec}(\mathbf{Y})\|_{\text{RMS}}] = \Omega(\|\mathbf{W}\|_F / \sqrt{D_{\text{out}}})$ .

Combining the two bounds gives  $\mathbb{E}_{\mathbf{X}} [\|\text{vec}(\mathbf{Y})\|_{\text{RMS}}] = \Theta(\|\mathbf{W}\|_F / \sqrt{D_{\text{out}}})$ . Setting  $\|\mathbf{W}\|_F = \Theta(\sqrt{D_{\text{out}}})$  yields the goal (20).  $\square$

## C.2.4 Practical Radius Selection

Combining Lemmas 3 and 4 with the norm-alignment relations of Oblique Manifolds definition in Section 2 yields a single tunable hyperparameter  $r = \Theta(1)$  that fixes all four radii simultaneously:

$$R_{\text{spec}} = r \sqrt{\frac{D_{\text{out}}}{D_{\text{in}}}}, \quad R_{\text{fro}} = r \sqrt{D_{\text{out}}}, \quad R_{\text{out}} = \frac{R_{\text{fro}}}{\sqrt{D_{\text{out}}}} = r, \quad R_{\text{in}} = \frac{R_{\text{fro}}}{\sqrt{D_{\text{in}}}} = r \sqrt{\frac{D_{\text{out}}}{D_{\text{in}}}}. \quad (42)$$

The mapping  $R_{\text{out}} = \|\mathbf{W}\|_F / \sqrt{D_{\text{out}}}$  and  $R_{\text{in}} = \|\mathbf{W}\|_F / \sqrt{D_{\text{in}}}$  follows directly from  $\|\mathbf{W}\|_F^2 = D_{\text{out}} R_{\text{out}}^2 = D_{\text{in}} R_{\text{in}}^2$  on the corresponding manifolds; these are the choices summarized in Table 1.

**Consistency with prior initialization schemes.** The radii in (42) agree with the initialization conventions of Yang et al. [20] and Wen et al. [11]. If the model is initialized as  $\mathbf{W}_0 \sim \mathcal{N}(0, \sigma^2)$  with  $\sigma = \min\left\{\sqrt{D_{\text{out}}/D_{\text{in}}}, 1\right\}/\sqrt{D_{\text{in}}}$ , then

$$\mathbb{E}[\|\mathbf{W}_0\|_F] \approx \sqrt{D_{\text{out}}D_{\text{in}} \text{Var}(\mathbf{W}_{ij})} = \min\left\{\sqrt{\frac{D_{\text{out}}}{D_{\text{in}}}}, 1\right\} \sqrt{D_{\text{out}}}, \quad (43)$$

which matches our Frobenius radius  $R_{\text{fro}} = r\sqrt{D_{\text{out}}}$  for  $r = \min\{\sqrt{D_{\text{out}}/D_{\text{in}}}, 1\} = \Theta(1)$ . Likewise, the data-dependent strategy of Wen et al. [11] fixes the radius to the realized energy of an  $\mathcal{N}(0, 1/D_{\text{out}})$  initialization, which corresponds to  $r = 1$  in (42).

### C.3 Rotational Equilibrium under Frobenius Sphere in Section 4.3

This subsection supplies a formal derivation of the Frobenius rotation identity stated in the main body (Section 4.3, paragraph on static rotational equilibrium under the Frobenius sphere) that does *not* rely on the heuristic Frobenius-norm-preservation argument used there. The argument is parametrized by the geometric *tangency cosine*

$$\alpha_t := \frac{\langle \mathbf{W}_t, O_t \rangle_F}{R \|O_t\|_F} = \cos \angle(\mathbf{W}_t, O_t) \in [-1, 1], \quad (44)$$

which is independent of  $\eta_t$  because  $O_t = \text{msign}(\Phi_t)$  depends on the gradient geometry alone.

**Setup.** On the Frobenius sphere  $\mathcal{M}_F(R) = \{\mathbf{W} : \|\mathbf{W}\|_F = R\}$ , the projection of any non-zero matrix  $A$  is  $\mathcal{P}_{\mathcal{M}_F}(A) = RA/\|A\|_F$ . With the normalized update direction  $\tilde{\nabla}_t = (cR/\|O_t\|_F)O_t$  used by MACRO,

$$\mathbf{W}_{t+1} = \mathcal{P}_{\mathcal{M}_F}(\mathbf{W}_t - \eta_t \tilde{\nabla}_t) = \frac{R}{\|\mathbf{W}_t - \eta_t \tilde{\nabla}_t\|_F} (\mathbf{W}_t - \eta_t \tilde{\nabla}_t), \quad (45)$$

and  $\|\mathbf{W}_t\|_F = \|\mathbf{W}_{t+1}\|_F = R$  by construction.

**Exact projected angle.** Direct computation yields

$$\langle \mathbf{W}_t - \eta_t \tilde{\nabla}_t, \mathbf{W}_t \rangle_F = R^2 - \eta_t c R^2 \alpha_t = R^2 (1 - \eta_t c \alpha_t), \quad (46)$$

$$\|\mathbf{W}_t - \eta_t \tilde{\nabla}_t\|_F^2 = R^2 - 2\eta_t c R^2 \alpha_t + \eta_t^2 c^2 R^2 = R^2 (1 - 2\eta_t c \alpha_t + \eta_t^2 c^2). \quad (47)$$

Combining (45)–(47),

$$\cos \theta_t = \frac{\langle \mathbf{W}_{t+1}, \mathbf{W}_t \rangle_F}{\|\mathbf{W}_{t+1}\|_F \|\mathbf{W}_t\|_F} = \frac{1 - \eta_t c \alpha_t}{\sqrt{1 - 2\eta_t c \alpha_t + \eta_t^2 c^2}}. \quad (48)$$

Equation (48) is exact in  $\eta_t$ ,  $c$ , and  $\alpha_t$ . No norm-preservation heuristic has been used; in particular, the inner product  $\langle \mathbf{W}_t, O_t \rangle_F$  enters only through the  $\eta_t$ -independent quantity  $\alpha_t$ .

**Taylor expansion.** Expanding the denominator of (48) via the binomial series  $(1+x)^{-1/2} = 1 - \frac{x}{2} + \frac{3x^2}{8} + O(x^3)$  with  $x = -2\eta_t c \alpha_t + \eta_t^2 c^2$  and retaining terms through  $O(\eta_t^2)$ ,

$$(1 - 2\eta_t c \alpha_t + \eta_t^2 c^2)^{-1/2} = 1 + \eta_t c \alpha_t - \frac{1}{2} \eta_t^2 c^2 + \frac{3}{2} \eta_t^2 c^2 \alpha_t^2 + O(\eta_t^3).$$

Multiplying by the numerator  $1 - \eta_t c \alpha_t$ , the  $O(\eta_t)$  terms cancel and we obtain

$$\cos \theta_t = 1 - \frac{1}{2} \eta_t^2 c^2 (1 - \alpha_t^2) + O(\eta_t^3). \quad (49)$$

Inverting via  $\arccos(1-z) \approx \sqrt{2z}$  for small  $z$  yields the rigorous Frobenius rotation identity

$$\boxed{\theta_t \approx \eta_t c \sqrt{1 - \alpha_t^2} = \eta_t c \sin \angle(\mathbf{W}_t, O_t)}. \quad (50)$$

Across our experiments the tangent-space residual for  $\mathcal{M}_F$   $\text{vio}(\mathbf{W}_t) := |\langle \mathbf{W}_t, \tilde{\nabla}_t \rangle|$  stabilizes at  $10^{-2}$ – $10^{-3}$  for every linear-layer type throughout training; see Figure 10 (Frobenius panel, right). Since  $|\alpha_t| = \text{vio}(\mathbf{W}_t)/cR^2$ , the same regime gives  $|\alpha_t| \approx 0$ , so

$$\sqrt{1 - \alpha_t^2} = 1 - \frac{1}{2} \alpha_t^2 + O(\alpha_t^4) \approx 1,$$

and (50) reduces to

$$\theta_t \approx \eta_t c, \quad (51)$$

which is the identity used in the main body and confirmed empirically by the flat curves of Figure 4.

**Contrast with the spectral case.** The same setup under the spectral norm requires Wedin’s sin  $\Theta$  theorem and produces an *adaptive* rotation angle modulated by the training-dependent spectral gap; see Appendix C.4. The contrast is geometric: the Frobenius-side rigorous identity (50) depends only on hyperparameters  $(\eta_t, c)$  and a small empirically-measured residual  $\alpha_t$ , whereas the spectral-side bound additionally depends on the iterate-dependent quantity  $R - \sigma_2(\mathbf{W}_{t+1})$ , producing the adaptive, anisotropic dynamics visualized in Figure 5.

#### C.4 Rotational Equilibrium under Spectral Sphere in Section 4.3

This section supplies the formal proof of the spectral rotation bound stated in the main body (Section 4.3, paragraph “Adaptive Rotational Equilibrium under Spectral Sphere”). Concretely, we show that under the normalized update rule of MACRO, the leading left and right singular subspaces of  $\mathbf{W}_t$  rotate by an angle whose magnitude is governed by the local spectral gap of  $\mathbf{W}_t$ . The argument relies on (i) the standard equivalence between subspace distance and principal angles (Appendix C.4.2), and (ii) the Wedin sin  $\Theta$  theorem for singular subspaces (Appendix C.4.3). The two ingredients are then combined in Appendix C.4.4.

##### C.4.1 Setup: Normalized Update on the Spectral Sphere

We start from the update step without projection step such as

$$\widetilde{\mathbf{W}}_{t+1} = \mathbf{W}_t - \eta_t \frac{c R O_t}{\|O_t\|_{\mathcal{M}}}, \text{ and } \mathbf{W}_{t+1} = \mathcal{P}_{\mathcal{M}_S}(\widetilde{\mathbf{W}}_{t+1})$$

where  $O_t$  is the (un-projected) update direction returned by the optimizer,  $R$  is the constraint radius,  $c = \Theta(1)$  is the relative-update hyperparameter, and  $\|\cdot\|_{\mathcal{M}}$  denotes the manifold-specific norm. For the spectral sphere  $\mathcal{M} = \mathcal{M}_{\text{spec}}(R)$  we set  $\|\cdot\|_{\mathcal{M}} = \|\cdot\|_2$ , and we denote the spectral perturbation by

$$\mathbf{E}_t := \widetilde{\mathbf{W}}_{t+1} - \mathbf{W}_t = -\eta_t \frac{c R O_t}{\|O_t\|_2}, \quad \|\mathbf{E}_t\|_2 = \eta_t c R. \quad (52)$$

Below, Wedin’s theorem is applied to the pair  $(\mathbf{W}_t, \widetilde{\mathbf{W}}_{t+1})$ , and then we transfer the resulting principal-angle bound from  $(\mathbf{W}_t, \widetilde{\mathbf{W}}_{t+1})$  to  $(\mathbf{W}_t, \mathbf{W}_{t+1})$ .

**Remark 2** (Update activation control). *The same normalized update (C.4.1), combined with the input scale assumption  $\|\text{vec}(\mathbf{X})\|_{\text{RMS}} = \Theta(1)$ , also secures the second  $\mu P$  desideratum (Figure 8) on the activation update,*

$$\|\text{vec}(\Delta \mathbf{Y}_t)\|_{\text{RMS}} = \eta_t \left\| \text{vec}\left(\frac{c R O_t}{\|O_t\|_2} \mathbf{X}\right) \right\|_{\text{RMS}} = \Theta(1), \quad (53)$$

since  $c R \eta_t = \Theta(1)$  and the bracketed factor obeys exactly the bound established for  $\mathbf{Y}_t$  in Lemma 3. This is the appendix counterpart of the forward-pass analysis in Appendix C.2.

##### C.4.2 Subspace Distance and Principal Angles

The Frobenius rotation angle of the main body is well defined because  $\|\cdot\|_F$  is induced by an inner product. The spectral norm is not, and the natural object of study is instead the rotation of *singular subspaces*, measured through principal angles.

**Definition 1** (Subspace distance and principal angles). *Let  $X, Z \in \mathbb{R}^{m \times r}$  have orthonormal columns ( $X^\top X = Z^\top Z = \mathbf{I}_r$ ). The subspace distance between  $\text{range}(X)$  and  $\text{range}(Z)$  is*

$$\text{dist}(X, Z) := \|X X^\top - Z Z^\top\|_2. \quad (54)$$

*Let  $X^\top Z = U \Sigma V^\top$  be the singular value decomposition of  $X^\top Z$ , and write  $\Sigma = \text{diag}(\sigma_1, \dots, \sigma_r)$  with  $1 \geq \sigma_1 \geq \dots \geq \sigma_r \geq 0$ . The principal angles  $\theta_1, \dots, \theta_r \in [0, \pi/2]$  between  $\text{range}(X)$  and  $\text{range}(Z)$  are defined by  $\cos \theta_i = \sigma_i$ .*

**Lemma 5** (Subspace distance and the largest principal angle). *For  $X, Z \in \mathbb{R}^{m \times r}$  with orthonormal columns,*

$$\text{dist}(X, Z) = \max_{1 \leq i \leq r} \sin \theta_i = \sin \theta_{\max}. \quad (55)$$

*Proof.* This is Stewart and Sun [66, Theorem I.5.5]. We give the short argument for completeness. Complete  $X$  and  $Z$  to orthogonal matrices  $[X \ X_\perp]$  and  $[Z \ Z_\perp]$  in  $\mathbb{R}^{m \times m}$ , so that

$$X X^\top - Z Z^\top = X X^\top (I - Z Z^\top) - (I - X X^\top) Z Z^\top = X (X^\top Z_\perp) Z_\perp^\top - X_\perp (X_\perp^\top Z) Z^\top. \quad (56)$$

The two terms have orthogonal column spaces and orthogonal row spaces, so

$$\|X X^\top - Z Z^\top\|_2 = \max\{\|X^\top Z_\perp\|_2, \|X_\perp^\top Z\|_2\}. \quad (57)$$

Each of these two operator norms equals  $\sin \theta_{\max}$ : indeed, the singular values of  $X^\top Z$  are  $\cos \theta_1, \dots, \cos \theta_r$ , hence those of  $X^\top Z_\perp$  are  $\sin \theta_1, \dots, \sin \theta_r$  (e.g., 66, Thm. I.5.2), and likewise for  $X_\perp^\top Z$ . The maximum singular value is therefore  $\sin \theta_{\max}$ , which proves (55).  $\square$

### C.4.3 Wedin's $\sin \Theta$ Theorem

We use the singular-vector form of the Davis–Kahan / Wedin perturbation theorem.

**Theorem 2** (Wedin  $\sin \Theta$  theorem; 32, see also 31, 66). *Let  $A, \tilde{A} \in \mathbb{R}^{m \times n}$  with  $\tilde{A} = A + E$ , and let*

$$A = [U_0 \ U_1] \begin{bmatrix} \Sigma_0 & \\ & \Sigma_1 \end{bmatrix} \begin{bmatrix} V_0^\top \\ V_1^\top \end{bmatrix}, \quad \tilde{A} = [\tilde{U}_0 \ \tilde{U}_1] \begin{bmatrix} \tilde{\Sigma}_0 & \\ & \tilde{\Sigma}_1 \end{bmatrix} \begin{bmatrix} \tilde{V}_0^\top \\ \tilde{V}_1^\top \end{bmatrix} \quad (58)$$

*be partitioned SVDs in which  $\Sigma_0, \tilde{\Sigma}_0$  collect the top  $r$  singular values and  $U_0, V_0, \tilde{U}_0, \tilde{V}_0$  have  $r$  orthonormal columns. Define the spectral gap*

$$\Delta := \min_{i \leq r, j > r} |\sigma_i(A) - \sigma_j(\tilde{A})|. \quad (59)$$

If  $\Delta > 0$ , then

$$\max\{\text{dist}(\tilde{U}_0, U_0), \text{dist}(\tilde{V}_0, V_0)\} \leq \frac{\max\{\|EV_0\|_2, \|E^\top U_0\|_2\}}{\Delta} \leq \frac{\|E\|_2}{\Delta}. \quad (60)$$

We will apply Theorem 2 to  $A = \mathbf{W}_t, \tilde{A} = \mathbf{W}_{t+1}$ , and the perturbation  $E = \mathbf{E}_t$  from (52).

### C.4.4 Proof of the Spectral Rotational Equilibrium Bound

We now combine Lemma 5 and Theorem 2 to bound the principal rotation angles between consecutive iterates on the spectral sphere. Let

$$\mathbf{W}_t = [\mathbf{U}_t^0 \ \mathbf{U}_t^1] \begin{bmatrix} \Sigma_t^0 & \\ & \Sigma_t^1 \end{bmatrix} \begin{bmatrix} \mathbf{V}_t^{0\top} \\ \mathbf{V}_t^{1\top} \end{bmatrix}, \quad \mathbf{W}_{t+1} = [\mathbf{U}_{t+1}^0 \ \mathbf{U}_{t+1}^1] \begin{bmatrix} \Sigma_{t+1}^0 & \\ & \Sigma_{t+1}^1 \end{bmatrix} \begin{bmatrix} \mathbf{V}_{t+1}^{0\top} \\ \mathbf{V}_{t+1}^{1\top} \end{bmatrix} \quad (61)$$

be partitioned SVDs in which  $\mathbf{U}^0, \mathbf{V}^0 \in \mathbb{R}^{D_{\text{out}} \times r}, \mathbb{R}^{D_{\text{in}} \times r}$  span the top- $r$  left and right singular subspaces, respectively. Set  $\mathbf{E}_t$  as in (52), so that  $\|\mathbf{E}_t\|_2 = \eta_t c R$ .

**General-rank bound.** Theorem 2 applied to  $A = \mathbf{W}_t, \tilde{A} = \mathbf{W}_{t+1}, E = \mathbf{E}_t$ , with the spectral gap

$$\Delta_r = \sigma_r(\mathbf{W}_t) - \sigma_{r+1}(\mathbf{W}_{t+1}) \quad (62)$$

(assumed strictly positive), yields

$$\max\{\text{dist}(\mathbf{U}_{t+1}^0, \mathbf{U}_t^0), \text{dist}(\mathbf{V}_{t+1}^0, \mathbf{V}_t^0)\} \leq \frac{\|\mathbf{E}_t\|_2}{\Delta_r} = \frac{\eta_t c R}{\Delta_r}. \quad (63)$$

By Lemma 5, the left-hand side equals the maximum sine of the principal angles, so

$$\max\{\sin \theta_{\max}^u, \sin \theta_{\max}^v\} \leq \frac{\eta_t c R}{\Delta_r}, \quad (64)$$

where  $\theta_{\max}^u$  (resp.  $\theta_{\max}^v$ ) is the largest principal angle between the top- $r$  left (resp. right) singular subspaces of  $\mathbf{W}_t$  and  $\mathbf{W}_{t+1}$ .

**Specialization to the leading direction.** The constraint  $\|\mathbf{W}_t\|_2 = R$  is active precisely on the leading singular value, so the strongest geometric restriction is on the top singular pair  $(\mathbf{u}_t, \mathbf{v}_t)$ . Setting  $r = 1$  and using  $\sigma_1(\mathbf{W}_t) = \sigma_1(\mathbf{W}_{t+1}) = R$ , the spectral gap (62) becomes

$$\Delta_1 = R - \sigma_2(\mathbf{W}_{t+1}), \quad (65)$$

and (64) reduces to

$$\max\{\sin \theta_u, \sin \theta_v\} \leq \frac{\eta_t c R}{R - \sigma_2(\mathbf{W}_{t+1})}, \quad (66)$$

where  $\theta_u = \arccos |\mathbf{u}_{t+1}^\top \mathbf{u}_t|$  and  $\theta_v = \arccos |\mathbf{v}_{t+1}^\top \mathbf{v}_t|$  are the angles between the leading singular vectors of consecutive iterates.

**Spectral effective learning rate.** Defining the spectral effective learning rate along the primary direction as  $\eta_{\text{eff}, t}^{\text{spec}} := \max\{\theta_u, \theta_v\}$ , the small-angle approximation  $\sin \theta \approx \theta$  (valid in typical training where  $\eta_t c R \ll \Delta_1$ ) converts (66) into

$$\boxed{\eta_{\text{eff}, t}^{\text{spec}} \lesssim \eta_t c \left( \frac{R}{R - \sigma_2(\mathbf{W}_{t+1})} \right)}. \quad (67)$$

The bound (67) is derived by applying Wedin's theorem to the pair  $(\mathbf{W}_t, \tilde{\mathbf{W}}_{t+1})$  rather than to  $(\mathbf{W}_t, \mathbf{W}_{t+1})$ . However, the projected iterate  $\mathbf{W}_{t+1} = \mathcal{P}_{\mathcal{M}_S(R)}(\tilde{\mathbf{W}}_{t+1})$  shares the singular subspaces of  $\tilde{\mathbf{W}}_{t+1}$  and preserves

$\sigma_j$  for every  $j \geq 2$ . Both the principal angles  $\theta_u, \theta_v$  and the spectral gap  $R - \sigma_2(\mathbf{W}_{t+1})$  are therefore identical when  $\widetilde{\mathbf{W}}_{t+1}$  is replaced by  $\mathbf{W}_{t+1}$ . The bound (67) consequently applies to the actual iterate produced by Algorithm 1, with no additional assumption.

This completes the proof of the spectral rotation bound stated in the main body. The contrast with the Frobenius case  $\eta_{\text{eff}, t}^{\text{frob}} \approx \eta_t c$  is geometric: under the Frobenius constraint the rotation angle is a function of hyperparameters alone, whereas under the spectral constraint it is modulated by the training-dependent spectral gap  $R - \sigma_2(\mathbf{W}_{t+1})$ , producing the adaptive, anisotropic dynamics empirically visualized in Figure 5.

## D Numerical Experiments Supplementary Materials

This appendix collects the implementation details for the experiments in Sections 4.2, 4.3, and 5. Across all experiments, the 1D parameters and the embedding layer are trained with AdamW under a fixed configuration: learning rate  $5 \times 10^{-3}$ ,  $\beta = (0.9, 0.95)$ , and  $\epsilon = 10^{-8}$ . To ensure a fair comparison, we fix the random seed across experiments. All experiments were conducted using  $8 \times$  NVIDIA H200 GPUs. The remaining parameters are trained with the optimizer specified in each experiment. We do not include wall-clock time comparison following the experiments setting in existing works. For example, SSO is implemented in Megatron which could accelerate its wall-clock time performance.

### D.1 Numerical Experiments Details in Section 4.2

**Experimental Setting.** We test whether MACRO can train a 330M-parameter Transformer to convergence with all learnable RMSNorm layers removed. The model is a QWEN3-like architecture with RoPE, GQA, and Norm-Gated SwiGLU, augmented by the parameter-free normalizations introduced in Section 4.2: a parameter-free RMSNorm after the attention block, QK-norm, and the Norm-Gated SwiGLU activation. Table 5 reports the full model and training configuration.

Category	Parameter	330M
<b>Model Configuration</b>	dimension	1024
	number of layers	24
	heads	16
	kv-heads	8
	sequence length	1024
	vocabulary size	50304
	Embedding Tie	True
<b>Train Configuration</b>	batch size	64
	gradient accumulation step	2
	lr schedule	linear warmup + cosine decay
	warmup steps	850
	cosine decay lr	$10^{-3} \times lr$
	Train Steps	8500
	# GPUs	8
	# Tokens	8.9B

Table 5: Model architecture and training configuration for the normalization-free 330M QWEN3-like experiment in Section 4.2.

**Hyperparameter Sweep and Selection.** For each of Muon, MACRO-spec, and MACRO-fro, we sweep the learning rate  $\eta_t$  over  $\{3 \times 10^{-3}, 5 \times 10^{-3}, 7 \times 10^{-3}, 1 \times 10^{-2}, 3 \times 10^{-2}\}$ . For the two constrained variants, we additionally sweep the radius hyperparameter  $r$  over  $\{0.7, 0.8, 0.9, 1.0, 1.1, 1.2, 1.3, 1.4, 1.5\}$ . Additionally, we also search qkv-split for MACRO-spec following [6]. Table 6 summarizes the search ranges, and Table 7 reports the per-optimizer hyperparameters that produce the bolded entries of Table 3 in the main text.

**Numerical Result Plots.** Figure 6 plots the training and validation loss across the 8500 training steps for all three optimizers at the chosen learning rate  $\eta_t = 10^{-2}$ , using the radii reported in Table 7. These curves give the per-step picture behind the best result in Table 3.

Optimizer	learning rate $\eta_t$	radius $r$	qkv-split
Muon	$[3 \times 10^{-3}, 3 \times 10^{-2}]$	-	-
MACRO-spec	$[3 \times 10^{-3}, 3 \times 10^{-2}]$	[0.7, 1.5]	[True, False]
MACRO-fro	$[3 \times 10^{-3}, 3 \times 10^{-2}]$	[0.7, 1.5]	-

Table 6: Hyperparameter search ranges for each optimizer in the normalization-free setting.

Parameter	Muon	MACRO-spec	MACRO-fro
learning rate $\eta_t$	0.01	0.01	0.01
weight decay	0.0	0.0	0.0
radius $r$	-	1.2	0.8
alignment $c$	-	1.0	1.0
qkv-split	-	False	-

Table 7: Selected hyperparameters per optimizer used to produce the bolded entries of Table 3.

**Ablation Study.** To validate the architecture design in Section 4.2, we run MACRO-spec while toggling three architectural choices: the activation (standard SwiGLU, Norm-Gated SwiGLU, or ReLU), the parameter-free RMSNorm after the attention block (Att-Norm), and the QK-norm. Each configuration is trained at three constraint radii  $r \in \{1.1, 1.2, 1.3\}$ . Table 8 reports the resulting validation loss. Standard SwiGLU diverges to NaN at every tested radius, even with both Att-Norm and QK-norm enabled. The Norm-Gated SwiGLU activation is the component that recovers stability, and adding Att-Norm and QK-norm on top yields the lowest validation loss across all three radii. ReLU is stable but underperforms Norm-Gated SwiGLU with both Att-Norm and QK-norm enabled.

## D.2 Numerical Experiments Details in Section 4.3

This subsection supplies the empirical evidence for the three claims of Section 4.3. First, the locked relative learning rate  $\eta_{rel,t} = c \eta_t$  produces a monotonically decaying global gradient norm under the cosine learning-rate schedule. Second, manifold constraints subsume the regularization role of decoupled weight decay. Third, the locked  $\eta_{rel,t}$  enables zero-shot Maximal Update Parametrization ( $\mu$ P) transfer across model widths. All experiments below reuse the QWEN3-like configurations summarized in Table 10.

**Gradient Norm Decay.** Equation (2) couples the relative update magnitude strictly to  $\eta_t$ , so the cosine decay of  $\eta_t$  translates directly into a decay of  $\eta_{rel,t}$ . Figure 7 plots the global gradient norm across the full

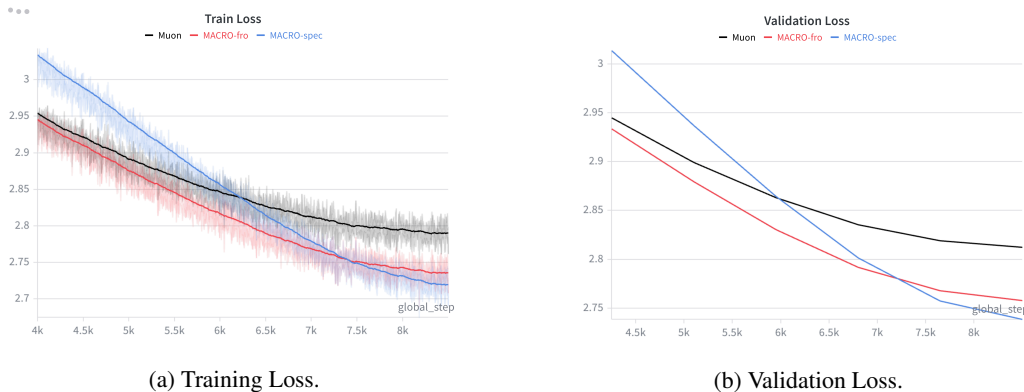


Figure 6: Training and validation loss for Muon, MACRO-fro, and MACRO-spec on the 330M QWEN3-like model with all learnable RMSNorm layers removed, at the chosen learning rate  $\eta_t = 10^{-2}$  (Table 7).

Activation	Att-Norm	QK-norm	$r = 1.1$	$r = 1.2$	$r = 1.3$
SwiGLU	True	True	NaN	NaN	NaN
Norm-Gated SwiGLU	False	False	2.76	2.762	2.77
Norm-Gated SwiGLU	True	False	2.747	2.746	2.749
Norm-Gated SwiGLU	True	True	2.744	2.742	2.743
ReLU	True	True	2.762	2.755	2.757

Table 8: Ablation Study on RMSNorm-free training

training schedule for both MACRO-spec and MACRO-fro at the 120M and 330M scales. In each panel, both curves drop from roughly  $3 \times 10^{-4}$  at the start of training to roughly  $10^{-5}$  at the end, without late-stage amplification. The figure confirms the main-body claim that locking  $\eta_{rel,t}$  avoids the late-stage gradient amplification that arises under heuristic weight-decay schedules [14].

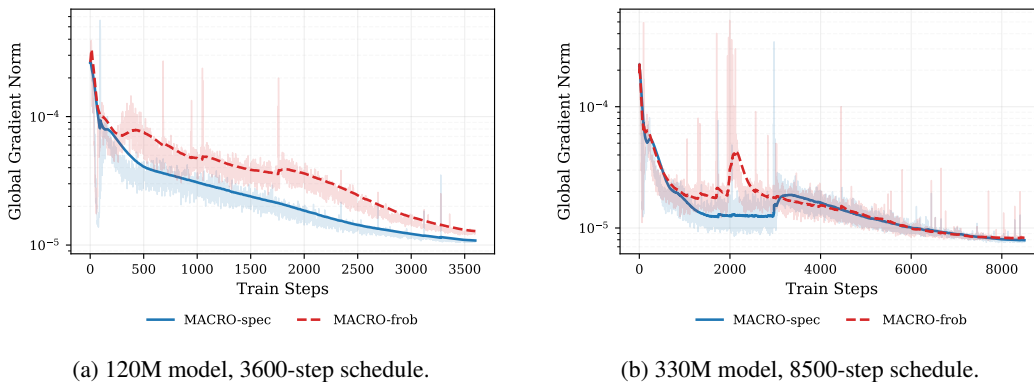


Figure 7: Global gradient norm across training for MACRO-spec (solid) and MACRO-fro (dashed) on the 120M and 330M QWEN3-like models from Table 10. Both curves decay monotonically from  $\sim 3 \times 10^{-4}$  to  $\sim 10^{-5}$ , consistent with the locked relative learning rate  $\eta_{rel,t} = c \eta_t$  tracking the cosine learning-rate schedule.

**Weight Decay Ablation.** Section 4.3 argues that manifold constraints subsume the regularization effect of decoupled weight decay. To verify this empirically, we train the 330M QWEN3-like model with each of MuonH-spec, MuonH-fro, MACRO-spec, and MACRO-fro under two settings:  $\lambda = 0.0$  (no weight decay) and  $\lambda = 0.1$ . We sweep the learning rate over  $\eta_t \in \{0.007, 0.01, 0.03\}$  and hold every other hyperparameter fixed at the values in Table 12. Table 9 reports the resulting validation loss. For every optimizer and every learning rate, the two  $\lambda$  settings agree within 0.001. Adding weight decay therefore has no measurable effect once a manifold constraint is active, which confirms the substitution claim.

**$\mu$ P Transfer.** The locked relative learning rate also enables zero-shot  $\mu$ P transfer across model widths. To make the experiment compatible with  $\mu$ P [20], we initialize the linear-layer weights from  $\mathcal{N}(0, \sigma^2)$  with  $\sigma = \min\{\sqrt{D_{out}/D_{in}}, 1\} / \sqrt{D_{in}}$  and set the Frobenius radius to  $R = r \min\{\sqrt{D_{out}/D_{in}}, 1\} \sqrt{D_{out}}$ , which absorbs the architecture-dependent  $\Theta(1)$  constant into the tunable hyperparameter  $r$  (see Section 4.1). For Spectral Sphere  $\mathcal{M}_R$  the radius is same with the radii in Section 4.1. Holding the rest of the 330M training configuration of Table 10 fixed, we vary the model width across  $\{256, 512, 1024, 2048\}$  and the learning rate across  $\{0.005, 0.007, 0.009, 0.01, 0.02, 0.03\}$ . Figure 8 reports the resulting validation loss for both MACRO-spec and MACRO-fro. Within each width, the validation-loss curve is nearly flat across the learning-rate sweep, and the minimum sits at the same learning rate ( $\eta_t \approx 0.01$  for MACRO-spec and  $\eta_t \approx 0.02$  for MACRO-fro) across all four widths. The locked  $\eta_{rel,t}$  therefore delivers zero-shot  $\mu$ P transfer in practice.

### D.3 Numerical Experiments Details in Section 5

**Experimental Setup.** Section 5 evaluates MACRO on QWEN3-like architectures at three scales: 120M, 330M, and 1B parameters. Each model uses RoPE, Grouped-Query Attention (GQA), and a SwiGLU activation, with pre-normalization RMSNorm placed before each residual block. We train every model on OpenWebText through

Optimizer	$\eta_t = 0.007$	$\eta_t = 0.01$	$\eta_t = 0.03$
MuonH-spec ( $\lambda = 0.0$ )	2.728	2.715	2.766
MuonH-spec ( $\lambda = 0.1$ )	2.729	2.715	2.766
MuonH-fro ( $\lambda = 0.0$ )	2.740	2.722	2.717
MuonH-fro ( $\lambda = 0.1$ )	2.740	2.722	2.717
MACRO-spec ( $\lambda = 0.0$ )	2.728	2.715	2.783
MACRO-spec ( $\lambda = 0.1$ )	2.727	2.715	2.783
MACRO-fro ( $\lambda = 0.0$ )	2.742	2.730	2.718
MACRO-fro ( $\lambda = 0.1$ )	2.742	2.729	2.718

Table 9: Weight-decay ablation on the 330M QWEN3-like model. Each manifold-constrained optimizer is trained with weight-decay coefficient  $\lambda \in \{0.0, 0.1\}$  at three learning rates  $\eta_t$ . Across every cell, the two  $\lambda$  settings differ by at most 0.001, which confirms that manifold constraints subsume the regularization role of decoupled weight decay. This phenomenon contradicts the Muon which benefits from weight decay widely reported in the literature.

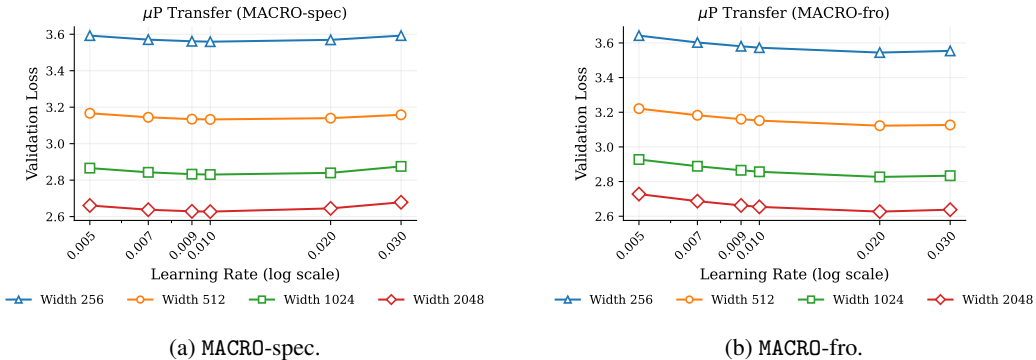
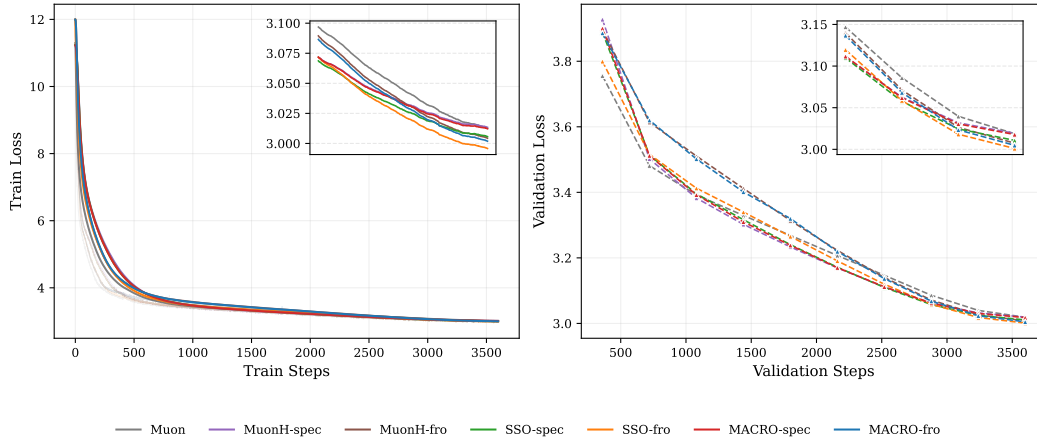


Figure 8: Validation loss versus learning rate at four model widths  $\{256, 512, 1024, 2048\}$  for the 330M QWEN3-like configuration of Table 10. Each width is trained with the same per-width radius  $r$  and the same alignment constant  $c$ . The optimum learning rate is consistent across widths, which empirically verifies zero-shot  $\mu$ P transfer for both MACRO-spec and MACRO-fro.

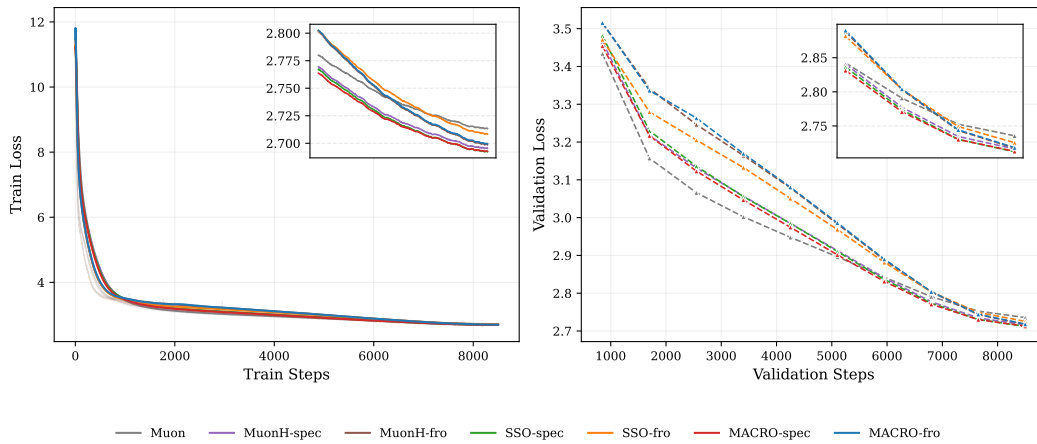
the NanoChat [67] codebase following the setup of Section 5. Across all scales, the 1D parameters and the embedding layer are trained with AdamW under the fixed configuration described at the start of this appendix. The remaining parameters are trained with the optimizer specified by each run. To ensure a fair comparison, we fix the random seed across runs. Table 10 reports the full model and training configuration.

**Hyperparameter Sweep and Selection.** We fix  $\beta_1 = 0.9$  for every optimizer. For the SSO and FSO double-loop solvers, we set the subproblem tolerance to  $10^{-4}$  and cap the inner-loop iterations at 10. For Muon, MACRO-spec, MACRO-fro, MuonH-spec, and MuonH-fro, we sweep the learning rate  $\eta_t$  over  $\{5 \times 10^{-3}, 7 \times 10^{-3}, 1 \times 10^{-2}, 3 \times 10^{-2}, 5 \times 10^{-2}\}$ . For the four manifold-constrained variants, we additionally sweep the constraint radius  $r$  over  $\{0.5, 1.0, 2.0, 5.0, 10.0\}$ . For MACRO-spec and MuonH-spec, we also sweep the qkv-split flag following [6]. The double-loop algorithms SSO and FSO are sensitive to compute cost, so we sweep only the learning rate and inherit the radius and qkv-split from the corresponding MuonH variant. Table 11 summarizes the search ranges, and Table 12 reports the chosen hyperparameters that produce the bold entries of Table 4 in the main text.

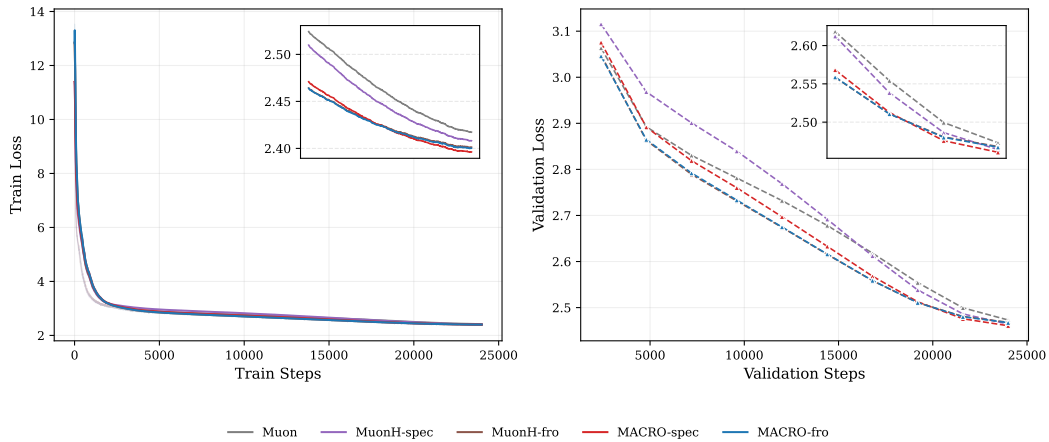
**Per-Step Training and Validation Loss Curves.** Figure 9 plots the training and validation loss across the full training schedule for each model scale. The curves give the per-step trajectory behind the final numbers reported in Table 4. All manifold-constrained optimizers (MACRO-spec, MACRO-fro, MuonH-spec, MuonH-fro, SSO, FSO) track the unconstrained Muon baseline closely throughout training, and they are superior than Muon in the late stage of training. Across the three scales, MACRO-spec and MACRO-fro reach validation losses comparable to the heuristic MuonH counterparts and to the exact double-loop SSO and FSO baselines.



(a) Train and Validation Loss for 120M training.



(b) Train and Validation Loss for 330M training.



(c) Train and Validation Loss for 1B training. SSO and FSO are omitted at this scale because of their double-loop computational cost (see Table 4).

Figure 9: Training (left) and validation (right) loss across the full training schedule for the 120M, 330M, and 1B QWEN3-like models. Each subfigure compares Muon, MuonH-spec, MuonH-fro, SSO, FSO, MACRO-spec, and MACRO-fro under the chosen hyperparameters from Table 12. These curves are the per-step trajectories underlying Table 4.

Category	Parameter	120M	330M	1B
<b>Model Config</b>	dimension	768	1024	2048
	number of layers	12	24	20
	heads	6	16	16
	kv_heads	3	8	8
	sequence length	1024	1024	1024
	vocabulary size	50304	50304	50304
	Embedding Tie	True	True	True
<b>Train Config</b>	batch size	128	64	16
	gradient accumulation step	1	2	16
	warmup steps	360	850	2400
	cosine decay lr	$10^{-3} \times lr$	$10^{-3} \times lr$	$10^{-3} \times lr$
	Train Steps	3600	8500	24000
	# GPUs	8	8	8
	# Tokens	3.7B	8.9B	50B

Table 10: Model architecture and training configuration for the 120M, 330M, and 1B QWEN3-like experiments in Section 5.

Optimizer	learning rate $\eta_t$	radius $r$	qkv-split
Muon	$[5 \times 10^{-3} - 5 \times 10^{-2}]$	-	-
MACRO-spec	$[5 \times 10^{-3} - 5 \times 10^{-2}]$	{0.5, 1.0, 2.0, 5.0, 10.0}	[False, True]
MACRO-fro	$[5 \times 10^{-3} - 5 \times 10^{-2}]$	{0.5, 1.0, 2.0, 5.0, 10.0}	-
MuonH-spec	$[5 \times 10^{-3} - 5 \times 10^{-2}]$	{0.5, 1.0, 2.0, 5.0, 10.0}	[False, True]
MuonH-fro	$[5 \times 10^{-3} - 5 \times 10^{-2}]$	{0.5, 1.0, 2.0, 5.0, 10.0}	-
SSO	$[5 \times 10^{-3} - 5 \times 10^{-2}]$	-	-
FSO	$[5 \times 10^{-3} - 5 \times 10^{-2}]$	-	-

Table 11: Hyperparameter search ranges for each optimizer in Section 5. The qkv-split sweep applies only to spectral-sphere variants, since the Frobenius constraint is invariant under the split. For SSO we follow [6] and fix qkv-split to True.

**Tangent Space Violation Ablation.** MACRO replaces the inner bisection of SSO and FSO with a single-step tangent space projection (Line 6 of Algorithm 1). To quantify the resulting trade-off, we measure the per-step tangent space violation, defined as the residual norm  $\text{vio}(\mathbf{W}_t) := |\langle \Gamma_t, \tilde{\nabla}_t \rangle|$  between the proposed update direction  $\tilde{\nabla}_t$  and the normal vector to the constraint surface  $\Gamma_t$  defined in Appendix B.1. Figure 10 reports the average of  $\text{vio}(\mathbf{W}_t)$  across the full 8500-step training schedule of the 330M model, separated by linear-layer type (FFN-Up, Attn-Out, Attn-Value, Attn-Query) and by manifold ( $\mathcal{M}_S$  on the left,  $\mathcal{M}_F$  on the right). Solid curves report MACRO; dashed curves report the corresponding exact double-loop solver (SSO for  $\mathcal{M}_S$ , FSO for  $\mathcal{M}_F$ ). Two conclusions follow.

First, MACRO keeps the absolute tangent space violation small. The solid curves stabilize at roughly  $10^{-3}$  to  $10^{-2}$  across all five layer types and both manifolds. The single-step projection therefore lands near, but not exactly on, the tangent space. The double-loop dashed curves stabilize at roughly  $10^{-4}$ , one to two orders of magnitude lower. Second, this larger residual does not translate into worse validation loss. Table 4 shows that MACRO-spec and MACRO-fro reach validation losses comparable to SSO and FSO on 120M model and 330M model. Removing the inner bisection therefore eliminates a large per-step computation overhead at no measurable cost in validation loss, and MACRO attains a favorable balance between tangent space residual and per-step computation.

Model	Optimizer	learning rate	weight decay	r	qkv-split
<b>120M</b>	Muon	0.03	0.1	-	-
	MuonH-spec	0.01	0.0	2.0	False
	MuonH-fro	0.03	0.0	1.0	-
	SSO	0.01	0.0	2.0	True
	FSO	0.03	0.0	1.0	-
	MACRO-spec	0.01	0.0	2.0	False
	MACRO-fro	0.03	0.0	1.0	-
<b>330M</b>	Muon	0.03	0.1	-	-
	MuonH-spec	0.01	0.0	2.0	False
	MuonH-fro	0.03	0.0	1.0	-
	SSO	0.01	0.0	2.0	True
	FSO	0.03	0.0	2.0	-
	MACRO-spec	0.01	0.0	2.0	False
	MACRO-fro	0.03	0.0	1.0	-
<b>1B</b>	Muon	0.01	0.1	-	-
	MuonH-spec	0.01	0.0	2.0	True
	MuonH-fro	0.01	0.0	1.0	-
	MACRO-spec	0.007	0.0	2.0	True
	MACRO-fro	0.01	0.0	1.0	-

Table 12: Selected hyperparameters per optimizer per model scale, used to produce the bold entries of Table 4 in the main text.

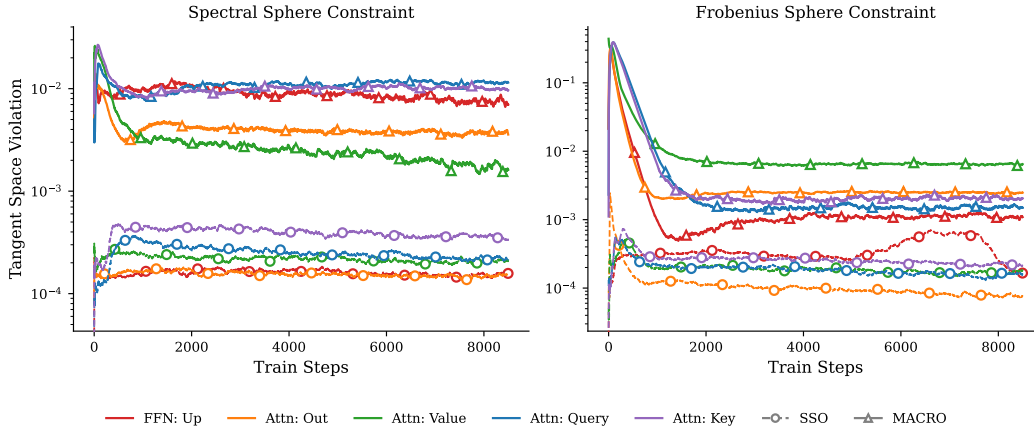


Figure 10: The average of Per-step tangent space violation  $\text{vio}(\mathbf{W}_t) := |\langle \Gamma_t, \tilde{\nabla}_t \rangle|$ , where  $\tilde{\nabla}_t$  is the update direction and  $\Gamma_t$  is the normal vector to the constraint surface, across the 8500-step training schedule of the 330M QWEN3-like model. The left panel reports the spectral sphere ( $\mathcal{M} = \mathcal{M}_S$ ); the right panel reports the Frobenius sphere ( $\mathcal{M} = \mathcal{M}_F$ ). Each colored curve corresponds to a linear-layer type (FFN-Up, Attn-Out, Attn-Value, Attn-Query, Attn-Key); solid curves report MACRO (single-step projection) and dashed curves report the corresponding exact double-loop solver (SSO for  $\mathcal{M}_S$ , FSO for  $\mathcal{M}_F$ ). Across all five layer types and both manifolds, MACRO stabilizes at residuals on the order of  $10^{-3}$  to  $10^{-2}$ , one to two orders of magnitude above the double-loop baseline. Table 4 shows that this larger residual does not degrade validation loss.

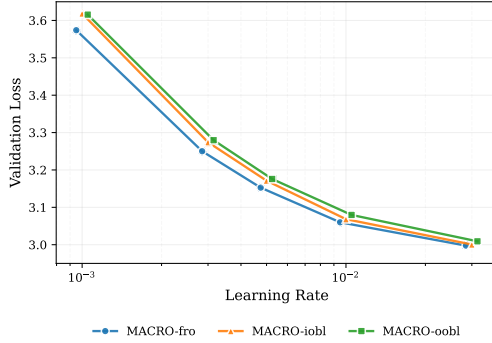
#### D.4 Empirical Equivalence of Oblique and Frobenius Constraints in Section 2

In Section 2, we introduced Oblique manifolds as candidates for row-wise or column-wise constraints. In this appendix, we provide the detailed empirical justification for omitting these Oblique constraints in favor of the Frobenius Sphere.

**Generalization Performance Advantage.** We first compare the generalization performance of the global Frobenius constraint ( $\mathcal{M}_F$ ) against the Input and Output Oblique constraints ( $\mathcal{M}_{O_{in}}$  and  $\mathcal{M}_{O_{out}}$ ). Figure 11 (a) plots the validation loss across various learning rates. The results show that the Frobenius constraint consistently achieves lower validation loss than both Oblique constraints. This clear performance gap provides the primary motivation for adopting the Frobenius sphere.

**Equivalence of Internal Training Dynamics.** To understand why Oblique constraints do not improve performance, we analyze the internal optimization dynamics. We specifically compare the global Frobenius constraint against the Input Oblique constraint. Figure 11 (b) and Figure 11 (c) track the spectral norm and the maximum row norm ( $2 \rightarrow \infty$  norm), respectively. For most learning rates, the trajectories under the Frobenius constraint closely match the trajectories under the explicitly normalized Input Oblique constraint. This matching behavior indicates that a Frobenius naturally regulates individual feature dimensions. The neural network implicitly maintains a uniform norm distribution without requiring strict row-wise or column-wise limitations.

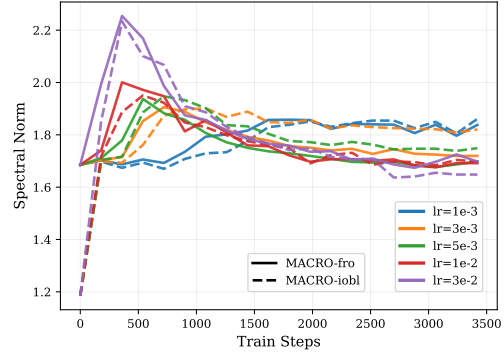
**Adaptive Capacity at Extreme Learning Rates.** While the dynamics are generally similar, Figure 11 (d) illustrates the maximum column norm ( $1 \rightarrow \infty$  norm) dynamics. At lower and standard learning rates, both constraints produce similar flat trajectories. However, at the highest learning rate ( $\eta = 3 \times 10^{-2}$ ), the trajectories separate. The Input Oblique constraint strictly limits the column norm, keeping the trajectory flat. In contrast, the Frobenius constraint allows this specific norm to adaptively increase. This flexibility suggests that the Frobenius sphere provides a better adaptive balance. It regularizes the overall weight matrix but allows specific feature dimensions to adapt when necessary. Because Oblique constraints offer no performance benefits and restrict this adaptive capacity, we omit them from our core theoretical and empirical analyses.



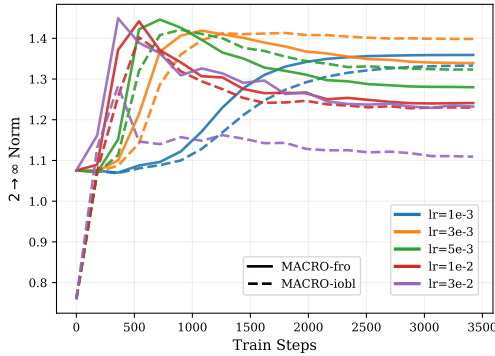
(a) **Validation loss across different learning rates.**

We compare the performance of MACRO-fro, MACRO-iobl, and MACRO-oobl. The x-axis represents the learning rate on a logarithmic scale.

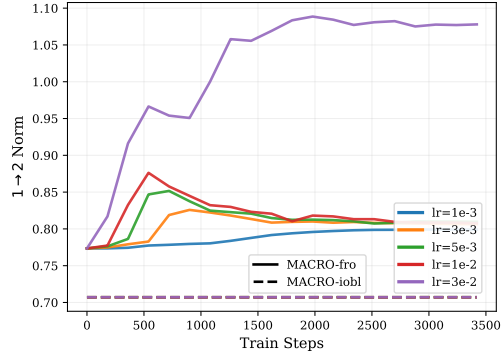
The global Frobenius constraint (MACRO-fro) consistently achieves the lowest validation loss across all evaluated learning rates compared to the Oblique constraints.



(b) **Spectral norm dynamics during training.** We track the spectral norm for MACRO-fro (solid lines) and MACRO-iobl (dashed lines) across five different learning rates. Despite the architectural differences between the constraints, the spectral norm trajectories remain highly similar throughout the training process.



(c) **Maximum  $2 \rightarrow \infty$  Norm dynamics.** We compare the  $2 \rightarrow \infty$  norm under the MACRO-fro and MACRO-iobl constraints. Similar to the spectral norm behavior, both constraints produce closely matching trajectories across the entire training period.



(d) **Maximum  $1 \rightarrow 2$  Norm dynamics.** We analyze the  $1 \rightarrow 2$  norm under the two constraints. For most learning rates, the trajectories match closely. However, at the learning rate  $\eta = 3 \times 10^{-2}$ , the Frobenius constraint allows the norm to increase, whereas the Input Oblique constraint strictly limits this growth.

Figure 11: Ablation study on geometric constraints.